The non–muscle actinopathy–associated mutation E334Q in cytoskeletal γ–actin perturbs interaction of actin filaments with myosin and ADF/cofilin family proteins

Johannes N. Greve[1], Anja Marquardt[1], Robin Heiringhoff[1], Theresia Reindl[1§], Claudia Thiel[1], Nataliya Di Donato[2], Manuel H. Taft[1], Dietmar J. Manstein[1,3,4,*]

1 Institute for Biophysical Chemistry, Hannover Medical School, Fritz–Hartmann–Centre for Medical Research, 30625 Hannover, Germany

2 Department of Human Genetics, Hannover Medical School, 30625 Hannover, Germany

3 Division for Structural Biochemistry, Hannover Medical School, 30625 Hannover, Germany

4 RESiST, Cluster of Excellence 2155, Hannover Medical School, 30625 Hannover, Germany

[§]Present address: Department of Microbiology and Immunology, Stanford University School of Medicine, 279 Campus Drive West, Stanford CA 94305, USA

*Corresponding author

Abstract

Various heterozygous cytoskeletal γ–actin mutations have been shown to cause Baraitser–Winter cerebrofrontofacial syndrome, non–syndromic hearing loss, or isolated eye coloboma. Here, we report the biochemical characterization of human cytoskeletal γ–actin carrying mutation E334Q, a mutation that leads to a hitherto unspecified non–muscle actinopathy. Following expression, purification, and removal of linker and thymosin β4 tag sequences, the p.E334Q monomers show normal integration into linear and branched actin filaments. The mutation does not affect thermal stability, actin filament nucleation, elongation and turnover. Model building and normal mode analysis predict significant differences in the interaction of p.E334Q–filaments with myosin motors and members of the ADF/cofilin family of actin–binding proteins. Assays probing the interactions of p.E334Q–filaments with human class 2 and class 5 myosin motor constructs show significant reductions in sliding velocity and actin–affinity. E334Q differentially affects cofilin-mediated actin dynamics by increasing the rate of cofilin-mediated *de novo* nucleation of actin filaments and decreasing the efficiency of cofilin-mediated filament severing. Thus, it is likely that p.E334Q-mediated changes in myosin motor activity, as well as filament turnover contribute to the observed disease phenotype.

Introduction

Cytoskeletal β– and γ–actin are the basic building blocks of the actin cytoskeleton in human non–muscle cells. The spatio–temporal regulation of these two actin isoforms, mediated by distinct actin–binding proteins (ABPs), drives the establishment and maintenance of specialized cytoskeletal compartments that are defined by their network architecture and the presence of specific filamentous actin–associated proteins (Pollard, 2016; Plastino & Blanchoin, 2019). The regulated ATP–dependent turnover of these actin networks as well as the coordinated interplay of actin with network–specific ABPs contribute to essential cellular processes like directed migration, adhesion, division and mechanotransduction (Ponti *et al*, 2004; Abercrombie *et al*, 1970, 1971; Ridley *et al*, 2003; Pollard *et al*, 2002; Lauffenburger & Horwitz, 1996).

β– and γ–actin differ by only four amino acids in the N–terminal region of the molecule but show isoform–specific spatial organization in studies performed with monoclonal antibodies. In motile and stationary cells, β–actin is found in contractile stress fibers and the cell periphery (Dugina *et al*, 2009; Latham *et al*, 2013; Dugina *et al*, 2015). In contrast, γ–actin localization is less static. During cell movement, γ–actin is recruited to the leading edge of the cell, resulting in an enrichment of the isoform in the lamellipodium together with β–actin (Dugina *et al*, 2009). In non–moving cell states, γ–actin is co–localized with β–actin in stress fibers (Dugina *et al*, 2009). In order to reconcile the highly similar protein sequences with the varying localization, several hypotheses on isoform regulation were put forward. These include the preferential interaction of ABPs with a particular isoform depending on the minor differences in the protein sequence, post–translational modifications as a means of isoform–specific regulation, and differences in the translation speed of *ACTB* and *ACTG1,* the genes encoding cytoskeletal β–actin and γ–actin (Zhang *et al*, 2010; Vedula *et al*, 2017; Pavlyk *et al*, 2018; Müller *et al*, 2013).

Diseases associated with heterozygous pathogenic variants in *ACTB* and *ACTG1* are typically referred to as non–muscle actinopathies. These include a spectrum of rare syndromes that manifest themselves as more or less pronounced developmental disorders in patients (Verloes *et al*, 2015; Di Donato *et al*, 2014; Latham *et al*, 2018; Rivière *et al*, 2012; Baraitser & Winter, 1988; Cuvertino *et al*, 2017). Baraitser–Winter–Cerebrontofacial–Syndrome (BWCFF, (Baraitser & Winter, 1988)) is a condition that affects the development of multiple organs, but particularly results in facial anomalies and brain malformations. BWCFF occurs due to various missense mutations in *ACTB* or *ACTG1* (Verloes *et al*, 2015; Di Donato *et al*, 2014; Rivière *et al*, 2012; Di Donato *et al*, 2016). BWCFF–patients show a recognizable facial gestalt, with variants in *ACTB* generally resulting in a stronger facial phenotype than mutations in *ACTG1* (Di Donato *et al*, 2014). BWCFF–patients regularly suffer from cortical malformations that lead to severe developmental and mental impairments. In addition, symptoms such as hearing loss, dystonia, hypotonia and polydactyly occur with increased frequency (Di Donato *et al*, 2014; Rivière *et al*, 2012). Variants in *ACTB* alone are responsible for two other well–defined syndromes. *ACTB*–associated pleiotropic malformation syndrome and *ACTB*–associated syndromic thrombocytopenia can be caused by single–point missense mutations, truncating mutations, frameshift mutations or deletion (Latham *et al*, 2018; Cuvertino *et al*, 2017). These *ACTB*–associated syndromes differ from BWCFF in that they cause only mild craniofacial malformations and developmental disorders (Cuvertino *et al*, 2017; Latham *et al*, 2018). Selected single–point missense mutations in *ACTG1* lead to a non–syndromic form of hearing loss (Rendtorff *et al*, 2006; van Wijk *et al*, 2003; Yuan *et al*, 2016).

How exactly mutations in the ubiquitously produced actin isoforms of the cytoskeleton lead to various syndromes and mutation-specific symptoms remains unclear. Currently, four main disease mechanisms are under discussion (Greve *et al*, 2022; Costa *et al*, 2004). First, mutations in the actin isoform can lead to functional haploinsufficiency, where the produced molecule is either intrinsically unstable and therefore degraded by the proteasome or unable to associate with other actin molecules and thus unable to partake in the necessary steps involved in the dynamic remodeling of the actin cytoskeleton. This results in a reduced amount of "active" actin molecules, which cannot fully be compensated for by the remaining allele (Vang *et al*, 2005). Second, the mutant protein is produced in normal quantities and integrated into filaments but interferes with actin filament turnover (Costa *et al*, 2004). Third, the mutation perturbs interactions with actin binding proteins, either by direct or allosteric disturbance of actin–actin or actin–ABP interaction interfaces (Greve *et al*, 2022; Hundt *et al*, 2014; Bryan *et al*, 2006; Müller *et al*, 2012). Fourth, the mutant protein shows an increased propensity for forming toxic rod–like oligomeric structures, which can potentially harm the cell (Ilkovski *et al*, 2004; Schröder *et al*, 2004).

Therefore, one of the significant challenges is elucidating the relationship between the disturbed molecular mechanisms of the cell's actin dynamics and disease patterns observed in patients. In order to achieve this, it is necessary to resolve the structure–function relationship of the various actin mutations at the molecular level. Here, we report the biochemical characterization of p.E334Q, a cytoskeletal γ–actin variant, which causes a syndromic form of non–muscle actinopathy. Features associated with the production of p.E334Q include mild facial anomalies and an abnormal gyral pattern of the cerebral cortex (Di Donato *et al*, 2016). At four years (age of diagnosis), a patient carrying this mutation showed developmental delay and severe muscle hypotonia (Di Donato *et al*, 2016). Although the patient was initially reported within the *ACTG1*–associated BWCFF cohort, careful reassessment of the phenotype revealed that the clinical phenotype cannot be classified as BWCFF and is therefore assigned as an unclassified NMA. Structural analysis of the disease–causing mutation shows that residue E334 is located in the hinge region of the actin molecule, which connects the two subdomain pairs of the protein. The region's flexibility and ability to act as a pivot point are essential for the subdomain rearrangement when actin monomers polymerize into filaments (**Figure 1A**). Furthermore, E334 is part of a contact region on the F–actin surface that interacts with the so-called cardiomyopathy–loop in the motor domain of cytoskeletal myosin isoforms and contributes to the formation of the actin–cofilin complex (**Figure 3**). We present experimental evidence for the impact of changes involving residue E334 with respect to productive interactions with cytoskeletal myosin isoforms, actin polymerization dynamics, and the formation of stable actin-cofilin complexes. We show that mutation E334Q does not adversely affect protein folding. The thermal stability of p.E334Q resembles that of the wild–type protein, both as a monomer and following integration into filaments. The mutant protein efficiently copolymerizes with wildtype (WT) monomers and integrates into linear and branched filament networks. In contrast, the interaction of mutant filaments with non-muscle myosin-2A/C and myosin-5A is strongly impaired, as shown by *in vitro* motility experiments and solution kinetics. Furthermore, p.E334Q filaments are less susceptible to cofilin–mediated disassembly, while monomers are more susceptible to cofilin–mediated nucleation.

Results

Production of cytoskeletal γ–actin and its variant p.E334Q

122 We produced untagged cytoskeletal γ–actin and its variant p.E334Q in insect cells, free of
123 contaminating endogenous *S. frugiperda* actin, using a method that was originally designed for the
124 production of toxic actin mutants in *Dictyostelium discoideum* and later adapted for use with the
125 baculovirus/Sf9 insect cell expression system (Noguchi *et al*, 2007; Lu *et al*, 2015). The monomeric actin
126 constructs were initially produced fused to the actin-monomer sequestering protein thymosin-β4.
127 Purification of the fusion protein by immobilized metal affinity chromatography, followed by
128 chymotrypsin–mediated cleavage of C–terminal linker and tag sequences, results in homogeneous
129 protein without non–native residues. The method worked equally well for both WT and mutant actin.
130 Starting with 2×10^9 cells, typical yields ranged from 5–7 mg of purified protein for cytoskeletal γ–actin
131 and p.E334Q (N=3 for WT and N=4 for p.E334Q).
132

133 ## Impact of mutation E334Q on protein folding and thermal stability

134 Mutation–induced misfolding of actin has been identified as one of the main causes for the
135 development of actinopathies (Bryan *et al*, 2006; Vang *et al*, 2005). Residue E334 is located in the hinge
136 region, formed by residues 137–145 and 333–338 (**Figure 1A**), which is strongly involved in the
137 structural reorganization of the monomer upon incorporation into a growing filament (Dominguez &
138 Holmes, 2011). Previous studies have shown that an intact hinge region is crucial for the interactions
139 with the eukaryotic chaperonin CCT/TriC and myosin (Noguchi *et al*, 2012; McCormack *et al*, 2001b,
140 2001a). We first performed a DNase–I inhibition assay to analyze the effect of mutation E334Q on the
141 folding of the protein. Previous studies have shown that the activity of DNase I is only effectively
142 inhibited by correctly folded actin (Schüler *et al*, 2000). We observed a 10% increase in the apparent
143 IC_{50}–value of p.E334Q (25.7± 0.6 nM) compared to the WT protein (22.7± 0.7 nM) (**Figure 1B)**. This is
144 in good agreement with CD–spectroscopy results showing nearly identical secondary structure
145 compositions for WT and mutant proteins (**Suppl. Figure 1**). Thermal denaturation temperatures (T_M)
146 analyzed by differential scanning fluorimetry (DSF) gave values of 56.77 ± 0.24°C and 56.19 ± 0.30°C
147 for monomeric WT actin and p.E334Q. The values obtained for WT and E334Q filaments were 65.00 ±
148 0.76°C and 64.83 ± 0.25°C, respectively (**Figure 1C, Table 1)**. Overall, these results show that the mutant
149 actin is correctly folded and has comparable stability to the WT protein.

150 As the hinge region is in close proximity to the nucleotide–binding cleft, we examined a potential effect
151 of the mutation on the interaction with nucleotides and the turnover of ATP. Initial tests gave near
152 identical rates of 0.00089 ± 0.00005 s^{-1} and 0.00088 ± 0.00004 s^{-1} for the steady–state turnover of ATP
153 by filaments formed from cytoskeletal γ–actin or the p.E334Q variant (**Table 1**). Next, we determined
154 the nucleotide dissociation rates k_{-T} and k_{-D} by monitoring the decrease in fluorescence amplitude
155 associated with the displacement of ε–ATP or ε–ADP after rapid mixing with a large excess of unlabeled
156 ATP. With p.E334Q-actin, we observed rates of k_{-T}=0.0972 ± 0.0019 s^{-1} and k_{-D}=0.3199 ± 0.0027 s^{-1}.
157 These rates are about 2-fold and 1.5-fold faster than those observed in experiments performed with
158 WT monomers (k_{-T}=0.0473 ± 0.0013 s^{-1}, k_{-D}= 0.2155 ± 0.0017 s^{-1} (**Figure 1D, Table 1**). The observed
159 nucleotide dissociation rates for human cytoskeletal γ–actin are in good agreement with values
160 obtained for a mixture of pyrene-labeled cytoskeletal γ–actin (15%) and β–actin (85%) purified from
161 human platelets in experiments performed at the same ionic strength (De La Cruz & Sept, 2010).

162

163 ## p.E334Q shows normal polymerization behavior and is efficiently integrated into
164 linear and branched actin structures

165 The regulated assembly and disassembly of filamentous actin drive various cellular processes, including
166 directed cell migration, adhesion and endocytosis. A slight conformational change of the actin
167 monomer accompanies the integration of a monomeric actin molecule into a growing filament. A small
168 change in the hinge region leading to a 12° to 13° rotation of the inner subdomain pair relative to the
169 outer subdomain pair results in a flatter actin molecule within the filament compared to the free actin
170 monomer (Dominguez & Holmes, 2011; Oda *et al*, 2009). Mutations in the hinge region can thus
171 potentially affect filament assembly by impairing the required structural reorganization of the
172 monomer, as it attaches to the growing filament end. TIRF microscopy–based tracking of the
173 polymerization of monomeric Atto–655–labeled WT or mutant actin *in vitro* revealed a small but
174 significant reduction in the elongation rate from 12.6 ± 0.3 nm s^{-1} for WT to 11.1 ± 0.3 nm s^{-1} for mutant
175 filaments (**Figure 2A, B**). To detect any differences in nucleation efficiency, we determined the time-
176 dependent increase in the number of filaments (**Figure 2C**). Aside from short-term fluctuations, the
177 linear increase in the number of filaments recorded for WT (0.039 ± 0.002 s^{-1}) and p.E334Q (0.041 ±
178 0.004 s^{-1}) was similar over the full 1000 s duration of the experiment. Overall, p.E334Q shows only a
179 mild polymerization defect.

180 Since actin polymerization *in vivo* is tightly regulated in a spatio–temporal manner by different ABPs,
181 we analyzed the interaction of p.E334Q with one of the key–regulators of actin polymerization, the
182 Arp2/3 complex (Goley & Welch, 2006). The Arp2/3 complex promotes the nucleation of new actin
183 filaments from the sides of existing filaments and caps their pointed ends. Thereby, it promotes the
184 formation of branched actin networks and contributes to essential processes that depend on the
185 dynamic remodeling of the actin cytoskeleton, such as cell migration, endocytosis, and organelle
186 positioning (Nicholson-Dykstra *et al*, 2005; Mullins *et al*, 1998; Blanchoin *et al*, 2000; Loisel *et al*, 1999).
187 The ability of p.E334Q to form branched actin networks was probed in TIRF microscopy–based
188 experiments in the presence of increasing concentrations of VCA–activated human Arp2/3 complex
189 (**Figure 2D**). At the lowest Arp2/3 concentration used (0.01 nM), we observed the appearance of the
190 first branches after approximately 250 s. In the presence of 0.1 nM and 0.2 nM of the VCA-activated
191 Arp2/3 complex, mutant and WT actin continued forming branched networks with comparable branch
192 formation and branch elongation rates. Similar results were obtained with WT actin, mutant actin or
193 with 1:1 mixtures of WT and mutant actin, when we analyzed the effect of adding increasing
194 concentrations of VCA–activated human Arp2/3 in pyrene–actin based bulk–polymerization assays
195 (**Figure 2E, F**). The results are summarized in **Table 1**.

196

197 Impact of E334Q mutation on interactions with ADF/cofilin family proteins

198 Homology models of the complexes formed by human cofilin–1 with filamentous cytoskeletal γ–actin
199 and p.E334Q were generated to evaluate the functional impact of mutation E334Q. Cofilin-1 binds to
200 actin filaments by making simultaneous contact with two adjacent monomers. Actin residue E334 is
201 located halfway between two adjacent cofilin molecules, but only makes direct contact with residue
202 L111 of the cofilin–1 molecule on the pointed end side (**Figure 3A**). Cofilin–1 residue L111 is located in
203 an α-helix (L111-L128) that is essential for actin–binding (Pope *et al*, 2000). Mutation E334Q maintains
204 the van der Waals interaction with L111, but reduces the electrostatic attraction between the
205 interacting surfaces, with likely effects on the stability and allosteric coupling of the complex (**Figure**
206 **3B, C**).

To evaluate the impact of mutation E334Q on the elastic properties of F–actin in the presence and absence of cofilin–1 binding, we performed normal mode analysis using bare, partially decorated and fully decorated filaments (**Suppl. Figure 2A**). Since residue E334 is located on the outer surface of the actin filament, the mutation produces no significant change in the normal mode frequencies of bare filaments. Similarly, fully decorated filaments show only minor differences. Substantial changes in the low-frequency modes associated with global conformational changes were observed when comparing the partially cofilin-decorated filaments of WT and mutant filaments, where the bare and cofilin–decorated regions move as rigid bodies and the interface between the two regions acts as a hinge (modes 7, 8) or fulcrum (mode 9) (**Suppl. Figure 2B**).

To test the validity of our modeling results, we performed biochemical and functional assays probing the interactions of human cofilin–1 with monomeric and filamentous cytoskeletal γ–actin and p.E334Q. The effect of cofilin–1 on filament assembly was assessed by TIRF microscopy experiments. The polymerization of 1 µM actin was induced in the presence of 0, 50 or 100 nM cofilin–1. Following an initial lag phase of 200 to 300 seconds, the filament formation rate increased with the cofilin–1 concentration (**Figure 4**). In experiments with p.E334Q-actin, *de novo* filament nucleation proceeded faster (**Figure 4A, B**). Movies showing filament formation by *de novo* nucleation in the presence of cofilin-1 are available in the supplement (**Suppl. Video 1–6**).

Next, we investigated the effect of cofilin–1 on the disassembly of preformed cytoskeletal γ–actin and p.E334Q filaments. The effect of cofilin–1 on existing WT and mutant filaments was initially tested by performing pyrene–based dilution–induced disassembly experiments with actin filaments polymerized for 16 hours and containing predominately ADP–actin. Cofilin–1 has previously been shown to increase the bulk–disassembly rate of actin in this experimental setup (Breitsprecher *et al*, 2011; Greve *et al*, 2022). In the absence of cofilin, the changes in pyrene–fluorescence are best described by single exponential functions with k_{obs} values of 0.0022 ± 0.0002 $s^{-1}$and 0.0029 ± 0.0003 s^{-1} for WT and p.E334Q filaments, respectively (**Figure 5A, Suppl. Figure 3**). The addition of cofilin–1 increased the observed rate of the dilution–induced disassembly in a concentration–dependent manner for both mutant and WT filaments. At the highest cofilin–1 concentration used (40 nM), the change in pyrene–fluorescence with p.E334Q filaments is still best described by a single exponential function with a k_{obs} value of 0.0059 ± 0.0008 s^{-1}. In contrast, the change for WT filaments is best-fitted to a bi-exponential function. Here, the k_{obs} values for the fast and slow phases are 0.0163 ± 0.0028 s^{-1} and 0.0002 ± 0.00003 s^{-1}, respectively (**Figure 5A, Suppl. Figure 3**). Additional experiments with heterofilaments showed milder but significant differences (**Table 1**).

The pyrene-based bulk experiments show an evident change in the p.E334Q-cofilin interaction. However, they cannot distinguish between changes affecting filament binding and filament disassembly. To analyze the perturbed interaction of p.E334Q with cofilin–1 in more detail, we first performed high-speed co–sedimentation assays with constant concentrations of F-actin (5 µM) and increasing concentrations of cofilin-1 (0.0625 – 20 µM) at pH 6.5 and pH 7.8. Cofilin-1 binds faster but severs filaments less efficiently under slightly acidic pH conditions, whereas a weakly basic environment favors cofilin–mediated severing (Wioland *et al*, 2019). We first performed experiments at pH 6.5. This endpoint experiment showed that cofilin–1 binds to and disassembles p.E334Q and WT filaments (**Figure 5B, C)**. Most pellet fractions from the experiments conducted with WT filaments were found to contain less cofilin-1, as higher disassembly efficiency results in more cofilin–1 being bound to actin monomers and retained in the supernatant fraction. We repeated the experiment at pH 7.8 with an equimolar and a 2–fold excess of cofilin, (**Figure 5B, C**). In experiments with equimolar cofilin–

1, we found significantly less WT actin in the pellet fraction than at pH 6.5, consistent with a higher disassembly–efficiency at pH 7.8. The shift to pH 7.8 did not have the same enhancing effect on the disassembly of p.E334Q filaments, as indicated by an increase of p.E334Q actin in the pellet fraction. The endpoint measurements show that cofilin–1 binds to p.E334Q filaments but severs them less efficiently. Next, we performed fluorescence quench experiments with pyrene-labeled WT and p.E334Q filaments, as it was previously shown that cofilin-1 efficiently quenches the fluorescence of pyrene-labeled actin filaments (Blanchoin & Pollard, 1999; De La Cruz, 2005). We determined the change in fluorescence amplitude when 2 µM pyrene-labeled p.E334Q or WT filaments were mixed with increasing concentrations of cofilin-1. Fitting a quadratic equation to the obtained experimental values gave only slightly different dissociation equilibrium constants of $K_{D,\ p.E334Q}$ = 1.83 ± 0.13 µM and $K_{D,\ WT}$ = 1.61 ± 0.07 µM (**Figure 5D**). These K_D values are in the range of values previously determined for muscle α-actin filaments (Blanchoin & Pollard, 1999; De La Cruz, 2005), actin filaments from *Acanthamoeba castellanii* (Blanchoin & Pollard, 1999) and filaments containing a mixture of human γ– and β–actin (De La Cruz, 2005) using the same method.

To better understand the underlying changes leading to the differences in cofilin–mediated filament disassembly efficiency, we performed two–color TIRF microscopy experiments using Atto–655 labeled WT or mutant filaments and eGFP–cofilin–1. This setup allows us to observe the binding of eGFP–cofilin–1 to individual filaments and the resulting disassembly of the filaments in real–time. eGFP–cofilin–1 was shown to bind to actin filaments and disassemble actin as efficiently as WT cofilin–1 (Wioland *et al*, 2019, 2017; Breitsprecher *et al*, 2011). Immediately after mixing 300 nM "aged" actin filaments, capped at their barbed end by human capping protein (CP), with 100 nM eGFP–cofilin–1, the reaction mixture was flushed into a flow–chamber and imaging was started. The delay between mixing and the start of imaging was approximately 15 seconds for each sample. At the end of the experimental dead time, almost twice as many cofilin clusters had formed in the field of view on WT filaments (151 ± 29) as on p.E334Q filaments (82 ± 6) (**Figure 6A**), the number of both WT and mutant actin filaments had doubled from initially about 95 to about 200 filaments (**Figure 6B**), and the Atto–655 fluorescence of the WT filaments had decreased to 30% of the starting value, whereas the Atto–655 fluorescence of p.E334Q filaments remained unchanged (**Figure 6C**). During the following 500 s, total eGFP-cofilin-1 fluorescence increased linearly, with the rate of increase being approximately twice as fast for WT as for p.E334Q filaments (**Figure 6D**). While the total eGFP-cofilin-1 fluorescence in the presence of p.E334Q filaments continued to increase linearly over the next 1000 seconds, the signal for WT filaments began to saturate and reached a plateau value (**Figure 6D**). The number of cofilin clusters on WT filaments decreased steadily during the observation period of 1500 s. In contrast, their number increased in the presence of p.E334Q filaments, reaching a maximum after 500 s, followed by a plateau of 400 s and a subsequent slow decrease (**Figure 6A**). The changes in the number of actin filaments showed similar time dependencies, a steady decrease for WT filaments and an initial increase for p.E334Q filaments followed immediately by a linear decrease without an intervening plateau phase (**Figure 6B**). For WT and p.E334Q filaments, the size of eGFP–cofilin–1 clusters on the steadily shrinking filaments expanded continuously until either severing occurred or the actin filament was fully decorated. No severing events were observed with fully decorated filaments.

Impact of E334Q mutation on interactions with myosin family proteins

The precise nature of the six actin-binding elements in the myosin motor domain varies considerably among myosin isoforms (Sellers, 2000; Cope *et al*, 1996). The associated sequences have conserved

295 hydrophobic and electrostatic properties, variations of which contribute to the tuning of kinetic and
296 functional properties. Actin residue E334 interacts with a positively charged patch in the
297 cardiomyopathy loop (CM–loop) of the myosin upper 50 kDa domain of NM2C and Myo5A (Pospich *et*
298 *al*, 2021; Von Der Ecken *et al*, 2016). In the case of NM2C, the electrostatic interaction of E334 with
299 K429 in the CM–loop is further stabilized by van der Waals interactions with I420 and V427 (**Figure 7**).
300 A lysine residue corresponding to K429 in NM2C is present in all human myosin–2 and myosin–5
301 isoforms. During force-generating interactions with mutant actin filaments, the weakening of
302 complementary electrostatic interactions in this region of the actomyosin interface is likely to
303 attenuate the binding affinity of class 2 and 5 myosins as well as the coupling between their actin and
304 nucleotide binding sites.

305 Cytoskeletal γ–actin filaments move with an average sliding velocity of 195.3 ± 5.0 nm s^{-1} on lawns of
306 surface immobilized NM2A–HMM molecules (**Figure 8A, B**). Filaments formed by p.E334Q actin move
307 5-fold slower, resulting in an observed average sliding velocity of 39.1 ± 3.2 nm/s. Filaments
308 copolymerized from a 1:1 mixture of WT and p.E334Q actin move with an average sliding velocity of
309 131.2 ± 10 nm s^{-1} (**Figure 8A, B**).

310 While we observed similar densities of surface-attached WT and mutant filaments, we noticed
311 increased rapid dissociation and association events for p.E334Q filaments (**Suppl. Video 7-9**). This
312 prompted us to investigate the impact of the mutation on actomyosin–affinity using transient–kinetic
313 approaches. We determined the dissociation rate constants using a single–headed NM2A–2R construct
314 (**Figure 8C**). NM2A–2R is a constitutively active motor–domain construct generated by fusing the
315 motor–domain of NM2A to two spectrin–like repeats serving as a rigid lever arm extension (Anson *et*
316 *al*, 1996). The construct is ideally suited for the kinetic characterization of the NM2–isoforms (Heissler
317 & Manstein, 2011). The dissociation rate constant k_{-A} is 5.6–fold increased from 0.08 × 10^{-3} s^{-1} to 0.45
318 × 10^{-3} s^{-1} for NM2A–2R when p.E334Q filaments are used. A similar change from 0.31 × 10^{-3} s^{-1} to 1.70
319 × 10^{-3} s^{-1} was observed for the analogous NM2C–2R construct (**Figure 8D**). Next, we determined the
320 affinities of NM2A–2R for WT and p.E334Q filaments in the absence of nucleotide (K_A) and the presence
321 of saturating concentrations of ADP (K_{DA}). We performed affinity–titration experiments with pyrene–
322 labeled, phalloidin–stabilized filaments and NM2A–2R (Kurzawa & Geeves, 1996). The values
323 measured under rigor conditions show a 9.9-fold reduced affinity of NM2A–2R for p.E334Q filaments
324 (K_A = 16.9 ± 1.3 nM) compared to WT filaments (K_A = 1.7 ± 0.3 nM) (**Figure 8E**). When the experiment
325 was performed in the presence of saturating concentrations of ADP, we obtained values for K_{DA} of 353.0
326 ± 20.6 nM in the presence of p.E334Q filaments and 122.6 ± 11.4 nM with WT filaments (**Figure 8F**).
327 The apparent ATP–affinity ($1/K_1$) of NM2A in complex with WT and p.E334Q filaments showed no
328 significant differences (**Table 1**).

329 Next, we investigated the effects of the E334Q mutation on the motile activity of the processive motor
330 Myo5A. Since the lysine residue corresponding to K429 in the CM loop of NM2C is also present in all
331 human myosin 5 isoforms, the resulting changes in binding strength and thermodynamic coupling are
332 expected to reduce the motor activity of Myo5A upon interactions with p.E334Q filaments. Structural
333 studies have shown that the interaction between actin residue E334 and the CM-loop in the Myo5A
334 motor domain is maintained from the rigor to the ADP–bound state (Pospich *et al*, 2021). We
335 performed unloaded *in vitro* motility assays to evaluate the effect of the mutation on the interaction
336 with Myo5A–HMM. The rapid transition from weak to strong binding with a slow and rate-limiting ADP
337 release leading to a high working ratio (De La Cruz *et al*, 1999) allows the *in vitro* motility assay to be
338 performed on surfaces with a low motor density. In initial experiments, we found a Myo5A–HMM

339 surface density of 770 molecules μm^{-2} to be optimal for experiments with WT filaments. Movement
340 was steady and filament breaks were practically non–existent at 770 molecules μm^{-2}, while higher
341 surface densities led to increased filament breaks, resulting in rapid fragmentation. At all Myo5A–
342 HMM surface densities used, the sliding velocity was significantly reduced for p.E334Q compared to
343 WT filaments. In experiments with p.E334Q filaments, a 4-fold higher Myo5A–HMM surface density
344 was required to achieve a similar actin surface decoration and optimal motile activity. Furthermore,
345 filament breaks occurred less frequently, indicating a less efficient actomyosin interaction. The number
346 of moving filaments and their sliding velocity decreased sharply below surface densities of 770
347 molecules/μm^2 for WT filaments and 3100 molecules μm^{-2} for p.E334Q filaments. Below a surface
348 density of 380 Myo5A–HMM molecules μm^{-2}, no productive attachment events were observed with
349 p.E334Q filaments. Thus, mutation E334Q in cytoskeletal γ–actin leads to an impairment of the
350 interaction of the actin filament with Myo5A, similar to the changes observed with NM2A and NM2C,
351 but with additional manifestations specific to processive motors.

352

353 ## Discussion

354 At present, the exact pathogenesis of non-muscular actinopathies remains poorly understood. A
355 rigorous molecular characterization of the contribution of disturbances in actin dynamics, contractility
356 and transport processes is necessary to develop an understanding of the diverse disease patterns.

357 In the past, the functional characterization of disease–associated mutations in cytoskeletal γ–actin
358 focused on mutations p.T89I, p.K118N/M, p.E241K, p.T278I, p.P264L, p.P332A, and p.V370A, which all
359 cause non–syndromic hearing loss. Two mutants showed abnormal polymerization behavior, indicated
360 by a reduced polymerization rate (p.V370A) (Bryan *et al*, 2006) or an increased propensity for bundle
361 formation (p.E241K) (Morín *et al*, 2009). The mutants p.K118N/M showed a perturbed interaction with
362 the Arp2/3 complex, reducing branching efficiency (Kruth & Rubenstein, 2012; Jepsen *et al*, 2016). A
363 significantly reduced protein stability was observed for two mutant proteins (p.P264L, p.P332A) (Bryan
364 *et al*, 2006). Perturbed interactions with cofilin were observed for a range of mutations. p.T89I,
365 p.E241K, p.T278I, and p.V370A are characterized by an increased sensitivity to cofilin–mediated
366 filament severing (Bryan & Rubenstein, 2009). Interestingly, mutation p.P332A, close to the analyzed
367 mutation p.E334Q, enhances resistance towards cofilin–mediated severing (Bryan & Rubenstein,
368 2009). The perturbed cofilin interaction is the only overlap between the spectrum of molecular
369 phenotypes observed for syndromic deafness–associated mutations and mutation p.E334Q, which
370 results in a non–syndromic actinopathy. It has to be noted that all cited studies relied on the use of
371 actin purified from budding yeast for their biochemical studies, which shows 91% sequence identity to
372 human cytoskeletal γ–actin (Ng & Abelson, 1980).

373 Here, we describe mutation E334Q in cytoskeletal γ–actin that leads to a syndromic actinopathy with
374 hypotonia and is not associated with non–syndromic hearing loss. Our biochemical analysis shows that
375 the mutation does not affect the folding of the actin monomer or the stability of the monomer and the
376 resulting filaments, demonstrating that mutations in the hinge region do not necessarily affect protein
377 stability. The mutant protein displays a robust interaction with the VCA-activated Arp2/3 complex. Its
378 polymerization kinetics are equivalent to those of the WT protein, with which it effectively
379 copolymerizes *in vitro*. Based on these observations, we exclude functional haploinsufficiency as a
380 potential disease mechanism and favor a mechanism in which p.E334Q integrates into the cytoskeletal
381 actin networks of the cell but shows defects in the interaction with key binding partners. Consistent

with this hypothesis and based on several structural studies (Pospich *et al*, 2021; Behrmann *et al*, 2012; Robert-Paganin *et al*, 2021; Risi *et al*, 2021; Fujii & Namba, 2017; Gyimesi *et al*, 2020; Gong *et al*, 2022; Gurel *et al*, 2017; Von Der Ecken *et al*, 2016) as well as our initial modeling of complexes formed by p.E334Q–filaments, we observed perturbed interactions with cofilin–1 and human cytoskeletal myosin isoforms NM2A, NM2C and Myo5A (**Table 1**).

We interpret the observed changes in the interaction with NM2A, NM2C and Myo5A to primarily reflect the weakening of complementary interactions between actin residue E334 and a core contact triad in the myosin CM–loop, which in the case of NM2C consists of K429 and hydrophobic residues I420 and V427 (**Figure 7**). Analogous changes in the interaction of mutant filaments with Myo1D, Myo1G, NM2B, Myo5B, Myo5C and Myo19 are expected due to the presence of the core contact triad residues in their CM–loops (**Figure 7B**). In contrast, the absence of a basic residue corresponding to K429 in NM2C and additional changes affecting their CM loop structure make it difficult to predict the consequences for the interaction of p.E334Q–filaments with the cytoskeletal myosin isoforms Myo1A, Myo1C, Myo1E, Myo1F, Myo3A, Myo3B, Myo15, Myo18A, Myo18B and Myo19.

In addition to primary consequences, reflected in the observed changes in the binding interactions with NM2A and cofilin–1, our results point to significant changes that result from allosteric perturbations. The results from our transient–kinetic analysis of the complexes formed by p.E334Q with NM2A–2R indicate that reduced allosteric coupling between the actin and nucleotide binding sites within the myosin motor domain contributes to the observed decrease in motor activity. The coupling efficiency is given by the ratio of the dissociation equilibrium constants for actin binding in the absence (K_A) and presence of ADP (K_{DA}). The value for K_{DA}/K_D obtained for the interaction of NM2A–2R in the presence of p.E334Q (20.9) is 3.5–fold lower than the value measured in the presence of WT actin (Table 1). Allosteric perturbations are also major contributors mediating the impact of mutation E334Q to the changes in elastic properties and the rate of actin filament disassembly in the presence of cofilin–1. Our results are consistent with the E334Q mutation slowing the initial complex formation due to less favorable charge interactions and allosteric perturbations having a major impact on subsequent steps.

Patients carrying mutations in *ACTB* or *ACTG1* predominately suffer from developmental disabilities, which can be directly linked to cortical malformations of varying severity. Therefore, neuronal cells and/or neuronal progenitor cells are assumed to be the most affected cell population in the patients (Verloes *et al*, 2015; Di Donato *et al*, 2016; Rivière *et al*, 2012). The actin composition of the neuron is thought to reach ratios between 1:1 and 1:2 for γ–actin to β–actin in the mature state after fluctuations during neuronal development (Cheever & Ervasti, 2013). Studies of the spatial localization of the cytoskeletal actin isoforms in the mature neuron are contradictory. A study showing that β– and γ–actin strongly colocalize in hippocampal and cerebral neurons (Cheever *et al*, 2012) appears to contradict previous studies, which reported spatial enrichment of β–actin in dynamic structures such as the dendritic spine and exclusion from less dynamic structures such as the axon shaft, where γ–actin was found to be enriched (Weinberger *et al*, 1996; Micheva *et al*, 1998; Bassell *et al*, 1998). Based on our results, we conclude that p.E334Q actin is readily produced and integrated into the cytoskeletal actin networks of neuronal cells, where it perturbs interactions with cytoskeletal myosin isoforms that play essential roles in the function and maintenance of healthy neurons. The functions of myosin-5 isoforms in neuronal cells are all linked to their role as actin barbed-end directed processive cargo transporters (Hammer & Wagner, 2013). Several of the myosin-5 driven transport-processes are important contributors to synaptic plasticity, i.e. the ability of the neurons to change synaptic strength based on previous activities (Hammer & Wagner, 2013).

426 The different NM2 isoforms are found in a wide range of cell types in the brain, but they show varying
427 spatial expressions (Murakami & Elzinga, 1992; Golomb *et al*, 2004; Rochlin *et al*, 1995; Kawamoto &
428 Adelstein, 1991). NM2A is predominately enriched in the vasculature of the brain, consistent with the
429 importance of NM2A for angiogenesis (Ma *et al*, 2020). NM2B and NM2C are mainly found in growth
430 cones and dendritic spines of neuronal cells (Murakami & Elzinga, 1992; Golomb *et al*, 2004; Rochlin *et*
431 *al*, 1995). NM2 isoforms are known to contribute to various neuronal processes, but unlike for Myo5A,
432 their exact role is less well understood. NM2B was shown to determine the maturation and
433 morphology of the dendritic spines in hippocampal neurons and was additionally linked to basal
434 synaptic function and plasticity (Hodges *et al*, 2011; Ma *et al*, 2004; Rex *et al*, 2010). NM2C and NM2B
435 contribute to the differentiation of oligodendrocytes (Domingues *et al*, 2020). The NM2 isoforms
436 compete with proteins of the ADF/cofilin family for binding to F–actin and this competition is essential
437 for stable actomyosin contractility and an intact cell cortex (Wiggan *et al*, 2012).

438 In line with this, ADF/cofilin family members are highly abundant in growth cones and dendritic spines
439 and essential for spine morphology and determination of spine length by modulating actin turnover
440 (Star *et al*, 2002; Hotulainen *et al*, 2009; Namme *et al*, 2021). Cofilin-mediated severing and nucleation
441 were previously proposed to synergistically contribute to global actin turnover in cells
442 (Andrianantoandro & Pollard, 2006; Du & Frieden, 1998). Our results show that the mutation affects
443 these different cofilin functions in actin dynamics in opposite ways. Cofilin-mediated filament
444 nucleation is more efficient for p.E334Q monomers, while cofilin-mediated severing of filaments
445 containing p.E334Q is significantly reduced. The interaction of both actin monomers and actin
446 filaments with ADF/cofilin proteins involves several distinct overlapping reactions. In the case of actin
447 filaments, cofilin binding is followed by structural modification of the filament, severing and
448 depolymerizing the filament (De La Cruz & Sept, 2010). Cofilin binding to monomeric actin is followed
449 by the closure of the nucleotide cleft and the formation of stabilized "long-pitch" actin dimers, which
450 stimulate nucleation (Andrianantoandro & Pollard, 2006).

451 While the number of disease–associated mutations reported for *ACTB* and *ACTG1* is steadily increasing,
452 the total number of patients affected remains low compared to patients with disease–associated
453 mutations in muscle actin isoforms (Parker *et al*, 2020). High sequence and structure conservation
454 across all actin isoforms enable us to extrapolate our findings obtained with cytoskeletal γ–actin to
455 diseases associated with mutations of E334 in other actin isoforms. Mutations of residue E334 in α–
456 skeletal actin (encoded by *ACTA1*) are reported to result in nemaline myopathy (E334K, (Laing *et al*,
457 2009)) or core myopathy (E334A, (Kaindl *et al*, 2004)) (reviewed in (Parker *et al*, 2020)). The mutations
458 either lead to the inversion of the charge at residue 334 (E334K) or the complete loss of charge (E334A).
459 Our study shows that loss of charge at actin residue 334 leads to the loss of a conserved core contact
460 between actin and the myosin motor domain of cytoskeletal class 2 myosin. Skeletal muscle myosin–2
461 is a central component of the sarcomere. The myosin forms the thick filaments that interact with the
462 thin filaments formed by actin and regulatory proteins, generating force that powers muscle
463 contraction (Sweeney & Hammers, 2018). Because the core contact triad that interacts with actin
464 residue E334 is present in all class 2 myosin isoforms, it is reasonable to assume that mutations of
465 residue E334 in α-skeletal actin affect the interaction with skeletal muscle myosin 2 to a similar extent,
466 resulting in less efficient force generation and thereby contributing to the development of myopathy
467 in patients.

468 Interestingly, a recent study analyzing the prevalence of cytoskeletal actin mutations in cancer using
469 the cBioPortal database found that mutations in *ACTB* and *ACTG1* are associated with lymphoid

470 cancers, specifically mutations in *ACTB* with diffuse large B–cell lymphoma and mutations in *ACTG1*
471 with multiple myeloma. When the authors extended the analysis to all cancer types, they found that
472 the observed mutations in the two genes were scattered across the entire actin sequence, with no
473 apparent preference for a particular region. Nevertheless, the group identified residue E334 in *ACTB*
474 as a potential hotspot, as the missense variants p.E334Q/p.E334K are more frequent in all analyzed
475 datasets (Witjes *et al*, 2020). In this paper, we investigated the impact of the E334Q exchange on the
476 function of cytoskeletal γ–actin in the context of developmental diseases. However, the high sequence
477 similarity between the cytoskeletal actin isoforms makes it highly likely that the E334Q mutation in
478 cytoskeletal β–actin results in similar molecular perturbations of actin dynamics but with potentially
479 different consequences for the organism due to varying enrichment of the two isoforms in functional
480 compartments of the actin cytoskeleton. Although future studies are needed to determine the role of
481 *ACTB* and *ACTG1* mutations as driver or passenger mutations in different cancers, our data show a
482 possible link between impaired cytoskeletal actomyosin dynamics, cofilin–mediated actin turnover and
483 cancer development.

484

485 # Material and Methods

486 ## Plasmids

487 The coding sequence of human cytoskeletal γ–actin (Uniprot-ID: P63261) was fused via a C–terminal
488 linker to a His_6–tagged thymosin β4 moiety (Uniprot-ID: P62328), as previously described for yeast
489 actin (Uniprot-ID: P60010) (Noguchi *et al*, 2007). The fusion protein was cloned into the multiple
490 cloning site of the pFastBac–Dual vector under the control of the polyhedrin promotor. The plasmid
491 encoding the mutant protein p.E334Q was generated by performing site-directed mutagenesis on the
492 WT plasmid. Motor domain carrying fragments of human NM2A, NM2C, and Myo5A were produced
493 using MYH9, MYH14, and MYO5A heavy chain sequences, respectively (Uniprot-IDs: P35579, Q7Z406,
494 Q9Y4I1). For the production of HMM-like constructs of human NM2A and human Myo5A, expression
495 vectors derived from pFastBac were used, as described previously (Hundt *et al*, 2016; Reindl *et al*,
496 2022). NM2A–HMM was co–produced with human light chains MYL6a (Uniprot-ID: P60660) and
497 MYL12b (Uniprot-ID: O14950). Myo5A HMM was co–produced with human calmodulin (Uniprot-ID:
498 P0DP23). NM2A–2R and NM2C–2R, single–headed, constitutively active motor domain constructs of
499 human NM2A and NM2C–2C0 with an artificial lever arm region, were produced using pFastBac–
500 derived expression vectors, as described previously (Heissler & Manstein, 2011; Müller *et al*, 2013).
501 Human cofilin–1 (Uniprot-ID: P23528) was cloned into the expression vector pGEX–6P–2 (Greve *et al*,
502 2022). The human Arp2/3 complex consisting of subunits Arp2 (Uniprot-ID: P61160), Arp3 (Uniprot-ID:
503 P61158), ArpC1B (Uniprot-ID: O15143, ArpC2 (Uniprot-ID: O15144), ArpC3A (Uniprot-ID: O15145),
504 ArpC4 (Uniprot-ID: P59998), ArpC5 (Uniprot-ID: O15511) and a C–terminal FLAG tag on ArpC3A was
505 produced using the expression vector pBIG2abc, provided by Roberto Dominguez (University of
506 Pennsylvania, Philadelphia, USA). The VCA domain of human N–WASP (Uniprot-ID: O00401) was
507 cloned into pGEX–6P–2. Human capping protein (subunits α1/β2, Uniprot-ID: P52907/P47756) in pET–
508 Duet–1 and eGFP–tagged human cofilin–1 (Uniprot-ID: P23528) in pGEX–6P–2 vector were provided
509 by Jan Faix (Medizinische Hochschule Hannover, Hannover, Germany). Recombinant bacmids and
510 viruses for the production of proteins in the Sf9 system were produced according to the *Bac–to–Bac*
511 baculovirus expression system protocol (Thermo Fisher Scientific, Waltham, MA, USA).

512

Protein production and purification

We produced recombinant human cytoskeletal γ–actin and p.E334Q mutant protein as actin–thymosin β4–His_6 fusion protein using the baculovirus/*S. frugiperda* insect cell expression system. The C-terminal native actin residue is a phenylalanine, which provides a cleavage site for chymotrypsin to remove downstream tag sequences completely. The tag sequence employed consists of a 14-amino acid linker (ASSGGSGSGGSGGA), 43 thymosin-β4 residues, followed by 6 histidine residues. To produce WT and mutant fusion proteins, 2×10^9 cells were harvested 72 hours after infection. Cells were pelleted, washed with PBS, shock frozen in liquid nitrogen and stored at –80 °C. Cell pellets from two liters of Sf–9 culture were thawed for a typical preparation. For lysis, cells were resuspended in lysis buffer–A (10 mM Tris pH 7.8, 5 mM $CaCl_2$, 10 mM imidazole, 1.25% Triton X–100, 100 mM KCl, 7 mM β–mercaptoethanol, 1 mM ATP, 1 mM PMSF, 100 µg/mL TAME, 80 µg/mL TPCK, 2 µg/mL pepstatin, 5 µg/mL leupeptin) and sonicated. The lysate was cleared by centrifugation at 30,000 × *g* (30 min, 4°C). The cleared lysate was loaded onto 3 mL equilibrated PureCube 100 NiNTA agarose (Cube Biotech, Manheim am Rhein, Germany) and incubated for two hours under constant rotation. Afterwards, the material was washed extensively with 10 mM Tris pH 7.8, 0.2 mM $CaCl_2$, 10 mM imidazole, 50 mM KCl, 1 mM ATP and the actin–thymosin β4 fusion protein was eluted with 10 mM Tris pH 7.8, 250 mM imidazole, 0.2 mM $CaCl_2$, 1 mM ATP. Peak fractions were pooled and dialyzed overnight against G–buffer (10 mM Tris pH 7.8, 0.2 mM $CaCl_2$, 0.1 mM ATP, 0.5 mM DTT). The next day, protein aggregates were removed by centrifugation at 15,000 × *g* (20 min, 4 °C). The supernatant was pooled and α–chymotrypsin (Sigma-Aldrich, Schnelldorf, Germany) was added at a w/w ratio of 1:300 (chymotrypsin:actin) to remove the tag-sequences. The optimal digestion time varied from 45 to 80 min and needs to be determined for each batch of α–chymotrypsin. PMSF was added to a final concentration of 0.2 mM to stop the digestion. Actin was separated from the thymosin-His tag using polymerization-depolymerization steps. Unless otherwise stated, all protein purification steps were carried out at 4°C. F-actin was stored on ice. G-actin was concentrated to approximately 150 µM, flash frozen in liquid nitrogen and stored at –80°C in G–buffer. Clarified G-actin, free of aggregates and oligomers, was always prepared fresh. G-actin stocks were thawed, diluted in G-buffer to the appropriate concentration, and centrifuged at 136,000 × *g* (15 min, 4°C). The top 2/3 of the centrifuged sample was carefully removed for use in further experiments. All myosin constructs were produced in the baculovirus/*S. frugiperda* insect cell expression system and purified as previously described for NM2A–HMM (Greve *et al*, 2022; Hundt *et al*, 2016; Pathan-Chhatbar *et al*, 2018), Myo5A–HMM (Reindl *et al*, 2022), the single–headed, constitutively active constructs NM2A–2R (Heissler & Manstein, 2011; Müller *et al*, 2013) and NM2C–2R (Heissler & Manstein, 2011; Müller *et al*, 2013). Production of the human Arp2/3 complex in insect cells followed the procedure described in Zimmet *et al*. (Zimmet *et al*, 2020). Human cofilin–1 and human eGFP–cofilin–1 were produced as GST–fusion proteins in Rosetta2 (DE3) cells. Purification was carried out as previously described for human cofilin–1 (Greve *et al*, 2022).

Human GST–N–WASP–VCA was produced in ArcticExpress (DE3) cells. The cells were lysed by treatment with lysozyme followed by sonification in lysis buffer–W (25 mM Tris pH 7.4, 50 mM NaCl, 1 mM EDTA, 1 mM DTT, 0.5% Triton X–100, 1 mM PMSF). The cleared cell lysate was loaded onto a self–packed GSH–Sepharose column. The column was then washed with five column volumes of wash buffer–W (25 mM TRIS pH 7.4, 50 mM NaCl, 1 mM EDTA, 1 mM DTT). GST–N–WASP–VCA was eluted from the column by applying 10 mM glutathione in wash buffer–W. The eluted protein was concentrated and loaded onto a S75 16/600 size exclusion chromatography column (GE Healthcare, Chicago, USA). After chromatography, fractions containing pure protein were pooled, concentrated

557 and the concentration was determined via absorbance at 280 nm. The GST–N–WASP–VCA protein was
558 frozen in liquid nitrogen and stored at – 80°C.

559 Human capping protein (α1/β2) carrying a 6×His–tag was produced in Rosetta2 (DE3) cells. For
560 purification, cells were lysed by lysozyme followed by sonification in lysis buffer-CP (25 mM Tris pH 7.8,
561 250 mM NaCl, 1 mM EDTA, 1 mM PMSF, 1.5 % Triton X–100, 10 mM imidazole, 7 mM beta–
562 mercaptoethanol). The cleared lysate was loaded onto PureCube 100 NiNTA agarose (Cube Biotech,
563 Monheim am Rhein, Germany) in a gravity–flow column. The agarose was washed with wash buffer–
564 CP (25 mM Tris pH 7.8, 250 mM NaCl, 30 mM imidazole) and the protein was then eluted with elution
565 buffer–CP (25 mM Tris pH 7.8, 50 mM NaCl, 250 mM imidazole). Fractions with pure capping protein
566 were pooled, concentrated and loaded onto a S200 16/600 size exclusion chromatography column (GE
567 Healthcare, Chicago, USA). The purified protein was frozen in liquid nitrogen and stored at –80°C.

568 α–skeletal actin (Uniprot-ID: P68139) was prepared from chicken pectoralis major muscle, as
569 previously described for rabbit α–skeletal actin (Lehrer & Kerwar, 1972).

570 Unless otherwise stated, all purification steps were performed at 4°C.

571

572 DNase–I inhibition assay, DSF and nucleotide exchange assay

573 The DNase–I inhibition assay and DSF to study actin folding and thermal stability were performed as
574 previously described (Greve *et al*, 2022).

575 Nucleotide exchange experiments were performed with freshly clarified G–actin as follows. The G–
576 actin solution was passed through a Zeba™ spin desalting column (Thermo Fisher Scientific, Waltham,
577 MA, USA) equilibrated with G–buffer to remove excess nucleotide. The sample was then incubated
578 with a 2–fold excess of ε–ATP or ε–ADP (Jena Bioscience, Jena, Germany) for two hours on ice. After
579 incubation, excess nucleotide was removed by passing the sample through a Zeba™ spin desalting
580 column equilibrated with 10 mM TRIS pH 8.0 and 10 µM ε–ATP/ ε–ADP. The concentration of the Ca^{2+}–
581 ε–ATP/ε–ADP–G–actin solution was determined using the Coomassie protein assay (Thermo Fisher
582 Scientific, Waltham, MA, USA). Prior to the nucleotide exchange experiment the Ca^{2+}–ε–ATP/ε–ADP–
583 G–actin solution was supplemented with 10× Mg^{2+}-exchange buffer (1 mM $MgCl_2$, 10 mM EGTA) to a
584 final concentration of 0.1 mM $MgCl_2$ and 1 mM EGTA. The resulting solution was rapidly mixed 1:1 with
585 assay buffer–SF containing excess unlabeled ATP (10 mM TRIS pH 7.8, 0.2 mM $MgCl_2$, 0.2 mM ATP)
586 using a HiTech Scientific SF61 stopped–flow system (TgK Scientific Limited, Bradford on Avon, UK). The
587 ε–ATP/ε–ADP fluorescence was excited at 335 nm and monitored through a KV389 cut–off filter. The
588 displacement of the fluorescent nucleotide analogs by ATP results in a decrease in the fluorescence
589 amplitude, which is best described by a single exponential fit that yields the apparent rate of nucleotide
590 dissociation

591

592 CD spectroscopy

593 Directly prior to the measurement, the freshly clarified G-actin was diluted to 0.05 mg/mL in 10 mM
594 phosphate buffer pH 7.4. A buffer reference was prepared by mixing G buffer with 10 mM phosphate
595 buffer pH 7.4 in the same ratio. CD spectroscopy was performed with a PiStar 180 spectrometer
596 (Applied Photophysics, Leatherhead, UK). Measurements were performed at 25°C using quartz
597 cuvettes (0.3 cm path length) and nitrogen purging. CD spectra were recorded from 176 nm to 280 nm

598 in steps of 1 nm using a bandwidth of 4 nm. For every sample, three spectra were recorded and
599 subsequently averaged. The averaged buffer spectrum was subtracted, and the resulting protein
600 spectrum smoothed using a Savitsky–Golay filter (Savitzky & Golay, 1964) in two consecutive iterations.
601 The DichroWeb online platform was used to determine the secondary structure composition
602 (Whitmore & Wallace, 2004). Data were analyzed based on the mean residue ellipticity $[\theta]_{\mathrm{MRE}}$ of the
603 sample using the CDSSTR algorithm and reference set 3 (optimized for 185 nm–240 nm).

604

605 Steady–state ATPase assay

606 The steady–state ATPase activity of F–actin was measured using a NADH–coupled enzymatic assay
607 (Furch *et al*, 1998). Experiments were performed with 10 µM F–actin at 37 °C in assay buffer–A (25 mM
608 HEPES pH 7.3, 5 mM $MgCl_2$, 50 mM KCl, 0.5 mM DTT) supplemented with the enzymatic system, which
609 generates the quantifiable readout (1 mM ATP, 0.5 mM NADH, 0.5 mM 2–phosphoenolpyruvate, 0.02
610 mg/mL lactate dehydrogenase from rabbit muscle (Sigma-Aldrich, Schnelldorf, Germany), 0.05 mg/mL
611 pyruvate kinase from rabbit muscle (Sigma-Aldrich, Schnelldorf, Germany), 0.5 mM NADH). The change
612 in absorbance at 340 nm due to oxidation of NADH was recorded in a Multiskan FC Microplate
613 Photometer (Thermo Fisher Scientific, Waltham, MA, USA).

614

615 TIRF microscopy–based assays

616 To distinguish between the impact of the mutation on filament nucleation and elongation, we
617 performed TIRF microscopy–based assays using freshly clarified protein. Unlabeled WT or mutant G–
618 actin was supplemented with 10% Atto–655 labeled WT or mutant G–actin for visualization of the
619 filament assembly process. Glass coverslips were cleaned, surfaces chemically treated and flow cells
620 assembled as described previously (Greve *et al*, 2022). To induce polymerization, the G–actin solutions
621 were diluted to a final concentration of 1 µM with 2× TIRF–buffer (20 mM imidazole, 50 mM KCl, 1 mM
622 $MgCl_2$, 1 mM EGTA, 0.2 mM ATP, 15 mM glucose, 20 mM β–ME, 0.25 % methylcellulose, 0.1 mg/mL
623 glucose oxidase and 0.02 mg/mL catalase. The solutions were mixed, immediately flushed into flow
624 cells and image acquisition was started.

625 To follow filament disassembly, two–color TIRF experiments with Atto–655 labeled actin and eGFP–
626 cofilin–1 were performed with preformed filaments that were "aged" and capped at their barbed end
627 by human capping protein. WT or mutant actin was polymerized for 3 hours at room temperature and
628 then moved to 4 °C overnight. "Aged" F–actin and human capping protein were diluted into TIRF–
629 buffer to generate capped actin filaments. eGFP–cofilin–1 was added to final concentrations of 300 nM
630 F–actin, 25 nM capping protein and 100 nM eGFP–cofilin–1. Immediately adding eGFP–cofilin–1, the
631 reaction mixture was flushed into the flow cell and image acquisition was started. Images were
632 captured using a Nikon Eclipse TI–E inverted microscope equipped with a 100×/1.49 NA Apo oil
633 immersion objective and Ixon3 897 EMCCD cameras (Andor, Belfast, UK) under control of the NIS
634 software (Nikon, Minato, Japan). Images were taken every 3 seconds with an exposure time of 60 ms.

635 To analyze actin polymerization in the presence of ABPs, the ABPs were first pre–diluted in KMEI buffer
636 and diluted to their final concentration in TIRF buffer just before adding actin. Image acquisition was
637 performed as described for experiments with actin only. Image analysis for all TIRF microscopy
638 experiments was performed using ImageJ (Rueden *et al*, 2017). The elongation rate of actin filaments
639 was determined by manually tracking individual filaments. Only filaments that could be tracked for at

640 least four consecutive minutes were used to determine the elongation rate. Using these criteria, 20 to
641 30 filaments were tracked in each individual experiment (in a microscopic field of view of 81.41 ×
642 81.41 µm). For quantification of two–color TIRFM–experiments, 52 × 52 µm ROIs from the entire
643 microscopic field of view were used. The number of filaments observed throughout an experiment was
644 determined using the *Analyze Particle* tool in ImageJ after background–subtraction (sliding paraboloid,
645 rolling ball radius: 25 pixels).

646

647 Unloaded *in vitro* motility assay

648 The unloaded *in vitro* motility assay to study the interaction between WT and mutant actin and NM2A–
649 HMM or Myo5A–HMM was essentially performed as previously described (Greve *et al*, 2022; Reindl *et*
650 *al*, 2022; Kron & Spudich, 1986). Flow cells used in the *in vitro* motility assay were constructed using
651 nitrocellulose–coated coverslips. NM2A–HMM requires phosphorylation of the associated regulatory
652 light chain for full enzymatic activity. Purified NM2A–HMM was incubated with the GST–tagged kinase
653 domain (residues 1425-1776) of human smooth muscle myosin light chain kinase (Uniprot-ID:
654 A0A8I5KU53) at a molar ratio of 10:1 in 25 mM MOPS, pH 7.3, 50 mM KCl, 5 mM $MgCl_2$, 1 mM $CaCl_2$,
655 0.2 µM calmodulin, 3 µM regulatory light chain (MLC12b), 3 µM essential light chain (MLC6a), 1 mM
656 DTT and 1 mM ATP for 30 minutes at 30 °C. In experiments with Myo5A–HMM, each buffer and actin
657 solution was supplemented with 2 µM calmodulin to prevent calmodulin dissociation from Myo5A–
658 HMM. Olympus IX70 or Olympus IX83 inverted fluorescence microscopes (Olympus, Hamburg,
659 Germany) equipped with a 60×/1.49 NA PlanApo oil immersion objective and an Orca Flash 4.0 CMOS
660 camera (Hamamatsu Photonics Deutschland GmbH, Herrsching, Germany) were used for image
661 acquisition. All *in vitro* motility experiments were performed at a 37°C. Analysis of the recorded image
662 series was performed in ImageJ (Rueden *et al*, 2017). The Plugin wrmTrck (Nussbaum-Krammer *et al*,
663 2015), developed by Jesper S. Pedersen, was used to determine the trajectories and corresponding
664 velocities of the individual actin filaments. Only filaments that showed movement for at least 30
665 consecutive seconds were tracked and used to determine the average sliding velocity.

666

667 Pyrene–actin based bulk–polymerization assays

668 The polymerization and depolymerization of pyrene–labeled recombinant WT or mutant actin (5%
669 pyrene-labeled WT or mutant actin) was monitored as a function of increasing or decreasing pyrene–
670 fluorescence using a Synergy 4™ microplate reader (BioTek Instruments, Winooski, VT, USA) and the
671 built–in filter set (Excitation: 340/30 nm, Emission: 400/30 nm) at 25 °C. For polymerization
672 experiments, 20 µL of a 10 µM solution of pyrene–labeled Mg^{2+}–ATP–G–actin (WT or mutant) was
673 placed in a black flat bottom 96–well plate (BrandTech Scientific, USA). 80 µL of 1.25 × polymerization
674 buffer (10 mM TRIS, pH 7.8, 100 mM KCl, 5 mM $MgCl_2$, 0.5 mM EGTA, 0.1 mM DTT and 0.1 mM ATP)
675 was added to the wells using the built–in pipetting function of the plate reader and the polymerization
676 of actin was followed as an increase in pyrene–fluorescence. For depolymerization experiments, 3 µL
677 of a 20 µM F–actin solution was placed in one well of the plate. The solution was rapidly diluted by the
678 addition of 297 µL G–buffer. The depolymerization of the filaments was monitored as a decrease in
679 pyrene–fluorescence.

680 The effects of Arp2/3 (+ GST–N–WASP–VCA) and cofilin–1 on filament assembly or disassembly were
681 analyzed by dispensing the actin solution and the ABP solution into the well by hand without mixing.

682 Polymerization buffer or G–buffer was added, the reaction components were thereby mixed and
683 recording of the ensuing changes in fluorescence intensity was started.

684 The bulk–polymerization rate was determined according to Doolittle *et al*. (Doolittle *et al*, 2013). A
685 linear regression was fitted to the linear region around the time–point of half–maximal fluorescence.
686 The depolymerization experiments were evaluated by fitting a single exponential function to the data,
687 including a linear component that accounts for bleaching.

688

689 Co–sedimentation experiments

690 Actin was polymerized at 20 µM for 3 hours at room temperature before being moved to 4 °C
691 overnight. For co–sedimentation experiments at pH 7.8, 5 µM of "aged" F–actin and varying
692 concentrations of human cofilin–1 were mixed in assay buffer–C (10 mM TRIS, pH 7.8, 100 mM KCl, 5
693 mM $MgCl_2$, 0.5 mM EGTA, 0.1 mM DTT and 0.1 mM ATP) to a final volume of 50 µL in 1.5 mL
694 polypropylene centrifuge tubes (Beckman Coulter, Brea, CA, USA) suited for high–speed centrifugation.
695 For experiments performed at pH 6.5, assay buffer–C was supplemented with piperazine–N,N'–bis(2–
696 ethanesulfonic acid) (PIPES, pH 6.5) to a final concentration of 100 mM to induce a pH shift from 7.8
697 to 6.5. Actin and cofilin–1 were added after the pH shift. Samples were incubated for 10 minutes at
698 23°C and then centrifuged at 136,000 × *g* (15 min, 4°C). The pellet and supernatant fractions were
699 subjected to SDS–PAGE and the gel was imaged at a ChemiDoc–MP–gel documentation system (Bio–
700 Rad Laboratories, Hercule, CA, USA). The amount of actin and cofilin–1 in the pellet and supernatant
701 was determined via densitometry using the Image Lab software (Bio–Rad Laboratories, Hercule, CA,
702 USA).

703

704 Transient kinetic analysis of the actomyosin complex

705 Myosin binding to pyrene–labeled actin leads to strong pyrene–fluorescence quenching. Mixing of the
706 rigor–pyrene–acto–NM2A–2R/NM2C–2R complex with an excess of unlabeled actin allows the
707 determination of k_{-A} (dissociation rate of myosin from F–actin in the absence of nucleotide). Prior to
708 the experiment, pyrene–labeled phalloidin–stabilized WT or mutant F–actin and the myosin solutions
709 were treated with apyrase (Merck KGaA, Darmstadt, Germany) to remove residual nucleotide. Pyrene–
710 labeled actin was mixed with a 1.5–fold excess of NM2A–2R/NM2C–2R in assay buffer–P (20 mM MOPS
711 pH 7.0, 100 mM KCl, 5 mM $MgCl_2$, 5 mM DTT) and incubated for 5 minutes on ice. The solution was
712 mixed with an excess of chicken α–skeletal actin in assay buffer–P to final concentrations of 0.5 µM
713 pyrene–labeled actin, 0.75 µM NM2A–2R and 5 µM α–skeletal actin. The solution was immediately
714 transferred into the well of a black 96–well microplate with a transparent bottom and a lid (Corning,
715 Corning, NY, USA). Fluorescence was excited at 365 nm and measured at 407 nm in a CLARIOstar Plus
716 microplate reader (BMG LABTECH, Offenburg, Germany) using bottom optics over 9 hours. The
717 dissociation rate (k_{-A}) of myosin from actin was determined by applying a single–exponential fit to the
718 data.

719 The apparent affinity of NM2A–2R to WT or mutant F–actin in the absence (K_A) or presence (K_{DA}) of
720 nucleotide was determined using the method developed by Kurzawa and Geeves (Kurzawa & Geeves,
721 1996). To determine K_A, all protein samples were treated with apyrase before the experiment. 100 nM
722 pyrene–labeled phalloidin–stabilized F–actin was incubated with increasing concentrations of NM2A–
723 2R (10–1,300 nM) for 5 minutes on ice in assay buffer–P without DTT. The solutions were shot against

724 20 µM ATP at a HiTech Scientific SF61 stopped–flow system (TgK Scientific Limited, Bradford on Avon,
725 UK) in a 1:1 ratio at 20 °C. Fluorescence was excited at 365 nm and recorded using a KV389 cut–off
726 filter. At least five transients were averaged for each concentration of NM2A–2R and fitted using a
727 single–exponential function. The relative fluorescence amplitudes were plotted against the pre–mix
728 myosin concentrations. The affinity was determined by applying a quadratic equation to the dataset,
729 where A is the amplitude, A_{max} the amplitude under saturation, [F–actin] the actin concentration prior
730 mix, [NM2A–2R] the variable NM2A–2R concentration and *K* the dissociation constant in the absence
731 or presence of nucleotide.

732 $$\mathrm{A} = \mathrm{A_{max}} \times ([\mathrm{F-Actin}] + [\mathrm{NM2A-2R}] + K) - \sqrt{\frac{([\mathrm{F-Actin}] + [\mathrm{NM2A-2R}] + K)^2 - 4 \times [\mathrm{F-Actin}] \times [\mathrm{NM2A-2R}]}{2 \times [\mathrm{F-Actin}]}}$$

733

734 Slight modifications of the experimental protocol were necessary to determine K_{DA}. Incubation with
735 apyrase was omitted, instead the pyrene–actomyosin complex was incubated with 30 µM ADP (Merck
736 KGaA, Darmstadt, Germany) for 20 minutes on ice prior to measurement. To account for the lower
737 affinity in the presence of ADP, the range of used myosin concentrations was extended up to 3,000
738 nM. Additionally, the concentration of ATP in the mixing experiment was increased to 300 µM pre–
739 mix. Data was recorded and evaluated as done for experiments without nucleotide.

740 The apparent ATP–affinity of the actomyosin complex was determined by mixing the apyrase–treated,
741 pyrene–labeled, phalloidin–stabilized actomyosin complex with increasing concentrations of ATP at
742 the stopped–flow system. Fitting an exponential function to the individual transients yields the ATP–
743 dependent dissociation rate of NM2A–2R from F–actin (k_{obs}). The k_{obs}–values were plotted against the
744 corresponding ATP concentrations and a hyperbola was fitted to the data. The fit yields the apparent
745 ATP affinity ($1/K_1$) of the actomyosin complex and the maximal dissociation rate.

746

747 Molecular modelling

748 Homology models of human cytoskeletal γ–actin, human cofilin–1 and the human NM2A motor
749 domain were generated with MODELLER (Sali & Blundell, 1993). Models of filamentous human
750 cytoskeletal γ–actin with bound cofilin–1 or NM2A motor domain were generated based on cryo–EM
751 structures obtained from the Protein Data Bank of the barbed end side of a cofilactin cluster (pdb:
752 6UC4, 6UBY, 6VAO) (Huehn *et al*, 2020) and a human cytoplasmic actomyosin complex (pdb: 5JLH)
753 (Von Der Ecken *et al*, 2016). The structures were accessed on May 25, 2023. Mutation E334Q was
754 introduced using the mutagenesis tool in PyMOL (Schrödinger, LLC, 2015). PyMOL and ChimeraX
755 (Goddard *et al*, 2018; Pettersen *et al*, 2021) were used for distance measurements and visualization of
756 Coulomb surfaces.
757 Identification and alignment of the CM–loop region of cytoskeletal myosin isoforms were performed
758 using the match function of ChimeraX, by superimposing and aligning cytoskeletal myosin isoform
759 structures on NM2C (pdb-NM2C: 5JLH, pdb-Myo5A: 7PM5, pdb-Myo5C: 5HMP, pdb-Myo1D: AF-
760 O94832-F1, pdb-Myo15: 7UDT, pdb-Myo19: AF-Q96H55-F1). Where appropriate, the corresponding
761 human sequences were retrieved from UniProt and structurally aligned.
762 Normal mode analyses (NMA) were performed using the Elastic Network Model (ENM) elNémo (Suhre
763 & Sanejouand, 2004) and an nrbl value of 5.
764

Data Analysis

Data analysis and graph plotting were performed with Origin 2023 (OriginLab Corporation. Massachusetts, USA). Errors are given as standard error of the mean (SEM) based on three independent experiments if not otherwise specified. The significance of the data was evaluated in Origin 2023 using a two–sample t–test ($p > 0.05 \triangleq$ ns, $p \leq 0.05 \triangleq$ *, $p \leq 0.01 \triangleq$ **, $p \leq 0.001 \triangleq$ ***, $p \leq 0.0001 \triangleq$ ****).

Author Contributions

All authors discussed the results and contributed to the final manuscript; J.N.G., T.R., C.T. purified proteins; J.N.G. performed experiments; A.M. and R.H. performed *in silico* studies; J.N.G. and D.J.M. analyzed the data; J.N.G., M.H.T., N.D.D. and D.J.M. contributed to the experimental design; J.N.G., A.M., R.H. and D.J.M. designed figures; J.N.G. and D.J.M. conceived and coordinated the study, and wrote the manuscript; D.J.M. was responsible for funding acquisition, supervision and project administration.

Acknowledgments

The authors thank Roberto Dominguez (University of Pennsylvania, Philadelphia, USA) for providing vector pBIGBac–Arp2/3 and Jan Faix (Medizinische Hochschule Hannover, Hannover, Germany) for providing vectors pGEX–eGFP–cofilin–1 and pETDuet–CP.

D.J.M was supported by grants from Deutsche Forschungsgemeinschaft (DFG) (MA1081/23-1, MA1081/28-1), J.N.G., A.M., N.DD and D.J.M. are members of the European Union's Horizon 2020 research and innovation program under the EJP RD COFUND–EJP N° 825575 with support from the German Federal Ministry of Education and Research under Grant Agreement 01GM1922B. D.J.M. is a member of the Cluster of Excellence RESIST (EXC 2155; DFG–Project ID: 39087428–B11). J.N.G. is supported by the HiLF I grant for early career researcher from Medizinische Hochschule Hannover. We gratefully acknowledge support provided by the Core Unit for Structural Biochemistry, the Core Unit for Laser Microscopy at MHH. Computing time was provided on supercomputers Lise and Emmy at NHR@ZIB and NHR@Göttingen, as part of the Alliance for National High Performance Computing (NHR) infrastructure. The calculations for this research were conducted with computing resources under the project ID nib00018. T.R. was enrolled in the PhD program Molecular Medicine of Hannover Biomedical Research School (HBRS).

Literature

Abercrombie M, Heaysman JEM & Pegrum SM (1971) The locomotion of fibroblasts in culture: IV. Electron microscopy of the leading lamella. *Exp Cell Res* 67: 359–367

Abercrombie M, Joan E, Heaysman M & Pegrum SM (1970) The locomotion of fibroblasts in culture: II. "Ruffling". *Exp Cell Res* 60: 437–444

Andrianantoandro E & Pollard TD (2006) Mechanism of Actin Filament Turnover by Severing and Nucleation at Different Concentrations of ADF/Cofilin. *Mol Cell* 24

Anson M, Geeves MA, Kurzawa SE & Manstein DJ (1996) Myosin motors with artificial lever arms. *EMBO J* 15: 6069–6074

Baraitser M & Winter RM (1988) Iris coloboma, ptosis, hypertelorism, and mental retardation: a new syndrome. *J Med Genet* 25: 41–43

Bassell GJ, Zhang H, Byrd AL, Femino AM, Singer RH, Taneja KL, Lifshitz LM, Herman IM & Kosik KS (1998) Sorting of beta-actin mRNA and protein to neurites and growth cones in culture. *J Neurosci Off J Soc Neurosci* 18: 251–265

Behrmann E, Müller M, Penczek PA, Mannherz HG, Manstein DJ & Raunser S (2012) Structure of the rigor actin-tropomyosin-myosin complex. *Cell* 150: 327–338

Blanchoin L, Amann KJ, Higgs HN, Marchand J-B, Kaiser DA & Pollard TD (2000) Direct observation of dendritic actin filament networks nucleated by Arp2/3 complex and WASP/Scar proteins. *Nature* 404: 1007–1011

Blanchoin L & Pollard TD (1999) Mechanism of interaction of Acanthamoeba actophorin (ADF/Cofilin) with actin filaments. *J Biol Chem* 274: 15538–15546

Breitsprecher D, Koestler SA, Chizhov I, Nemethova M, Mueller J, Goode BL, Small JV, Rottner K & Faix J (2011) Cofilin cooperates with fascin to disassemble filopodial actin filaments. *J Cell Sci* 124: 3305–3318

Bryan KE & Rubenstein PA (2009) Allele-specific effects of human deafness γ-actin mutations (DFNA20/26) on the actin/cofilin interaction. *J Biol Chem* 284

Bryan KE, Wen KK, Zhu M, Rendtorff ND, Feldkamp M, Tranebjaerg L, Friderici KH & Rubenstein PA (2006) Effects of human deafness γ-actin mutations (DFNA20/26) on actin function. *J Biol Chem* 281

Cheever TR & Ervasti JM (2013) Actin isoforms in neuronal development and function. *Int Rev Cell Mol Biol* 301: 157–213

Cheever TR, Li B & Ervasti JM (2012) Restricted Morphological and Behavioral Abnormalities following Ablation of β-Actin in the Brain. *PLoS ONE* 7: e32970

845 Cope MJT, Whisstock J, Rayment I & Kendrick-Jones J (1996) Conservation within the myosin motor
846 domain: implications for structure and function. *Structure* 4: 969–987
847
848 Costa CF, Rommelaere H, Waterschoot D, Sethi KK, Nowak KJ, Laing NG, Ampe C & Machesky LM
849 (2004) Myopathy mutations in alpha-skeletal-muscle actin cause a range of molecular defects. *J Cell Sci*
850 117: 3367–3377
851
852 Cuvertino S, Stuart HM, Chandler KE, Roberts NA, Armstrong R, Bernardini L, Bhaskar S, Callewaert
853 B, Clayton-Smith J, Davalillo CH, *et al* (2017) ACTB Loss-of-Function Mutations Result in a
854 Pleiotropic Developmental Disorder. *Am J Hum Genet*
855
856 De La Cruz EM (2005) Cofilin Binding to Muscle and Non-muscle Actin Filaments: Isoform-dependent
857 Cooperative Interactions. *J Mol Biol* 346: 557–564
858
859 De La Cruz EM & Sept D (2010) The Kinetics of Cooperative Cofilin Binding Reveals Two States of
860 the Cofilin-Actin Filament. *Biophys J* 98: 1893–1901
861
862 De La Cruz EM, Wells AL, Rosenfeld SS, Ostap EM & Sweeney HL (1999) The kinetic mechanism of
863 myosin V. *Proc Natl Acad Sci* 96: 13726–13731
864
865 Di Donato N, Kuechler A, Vergano S, Heinritz W, Bodurtha J, Merchant SR, Breningstall G, Ladda R,
866 Sell S, Altmüller J, *et al* (2016) Update on the ACTG1-associated Baraitser–Winter cerebrofrontofacial
867 syndrome. *Am J Med Genet A* 170
868
869 Di Donato N, Rump A, Koenig R, Der Kaloustian VM, Halal F, Sonntag K, Krause C, Hackmann K,
870 Hahn G, Schrock E, *et al* (2014) Severe forms of Baraitser-Winter syndrome are caused by ACTB
871 mutations rather than ACTG1 mutations. *Eur J Hum Genet* 22: 179–183
872
873 Domingues HS, Urbanski MM, Macedo-Ribeiro S, Almaktari A, Irfan A, Hernandez Y, Wang H, Relvas
874 JB, Rubinstein B, Melendez-Vasquez CV, *et al* (2020) Pushing myelination – developmental regulation
875 of myosin expression drives oligodendrocyte morphological differentiation. *J Cell Sci* 133: jcs232264
876
877 Dominguez R & Holmes KC (2011) Actin Structure and Function. *Annu Rev Biophys* 40: 169–186
878
879 Doolittle LK, Rosen MK & Padrick SB (2013) Measurement and analysis of in vitro actin
880 polymerization. *Methods Mol Biol* 1046
881
882 Du J & Frieden C (1998) Kinetic Studies on the Effect of Yeast Cofilin on Yeast Actin Polymerization.
883 *Biochemistry* 37: 13276–13284
884
885 Dugina V, Khromova N, Rybko V, Blizniukov O, Shagieva G, Chaponnier C, Kopnin B & Kopnin P
886 (2015) Tumor promotion by γ and suppression by β non-muscle actin isoforms. *Oncotarget* 6: 14556–
887 14571
888
889 Dugina V, Zwaenepoel I, Gabbiani G, Clément S & Chaponnier C (2009) Beta and gamma-cytoplasmic
890 actins display distinct distribution and functional diversity. *J Cell Sci* 122: 2980–8
891
892

Fujii T & Namba K (2017) Structure of actomyosin rigour complex at 5.2 Å resolution and insights into the ATPase cycle mechanism. *Nat Commun* 8: 13969

Furch M, Geeves MA & Manstein DJ (1998) Modulation of Actin Affinity and Actomyosin Adenosine Triphosphatase by Charge Changes in the Myosin Motor Domain. *Biochemistry* 37: 6317–6326

Goddard TD, Huang CC, Meng EC, Pettersen EF, Couch GS, Morris JH & Ferrin TE (2018) UCSF ChimeraX: Meeting modern challenges in visualization and analysis. *Protein Sci Publ Protein Soc* 27: 14–25

Goley ED & Welch MD (2006) The ARP2/3 complex: an actin nucleator comes of age. *Nat Rev Mol Cell Biol* 7: 713–726

Golomb E, Ma X, Jana SS, Preston YA, Kawamoto S, Shoham NG, Goldin E, Conti MA, Sellers JR & Adelstein RS (2004) Identification and characterization of nonmuscle myosin II-C, a new member of the myosin II family. *J Biol Chem* 279: 2800–2808

Gong R, Jiang F, Moreland ZG, Reynolds MJ, de los Reyes SE, Gurel P, Shams A, Heidings JB, Bowl MR, Bird JE, *et al* (2022) Structural basis for tunable control of actin dynamics by myosin-15 in mechanosensory stereocilia. *Sci Adv* 8: eabl4733

Greve JN, Schwäbe FV, Pokrant T, Faix J, Di Donato N, Taft MH & Manstein DJ (2022) Frameshift mutation S368fs in the gene encoding cytoskeletal β-actin leads to ACTB-associated syndromic thrombocytopenia by impairing actin dynamics. *Eur J Cell Biol* 101: 151216

Gurel PS, Kim LY, Ruijgrok PV, Omabegho T, Bryant Z & Alushin GM (2017) Cryo-EM structures reveal specialization at the myosin VI-actin interface and a mechanism of force sensitivity. *eLife* 6: e31125

Gyimesi M, Horváth ÁI, Túrós D, Suthar SK, Pénzes M, Kurdi C, Canon L, Kikuti C, Ruppel KM, Trivedi DV, *et al* (2020) Single Residue Variation in Skeletal Muscle Myosin Enables Direct and Selective Drug Targeting for Spasticity and Muscle Stiffness. *Cell* 183: 335-346.e13

Hammer JA & Wagner W (2013) Functions of Class V Myosins in Neurons. *J Biol Chem* 288: 28428–28434

Heissler SM & Manstein DJ (2011) Comparative kinetic and functional characterization of the motor domains of human nonmuscle myosin-2C isoforms. *J Biol Chem* 286: 21191–21202

Hodges JL, Newell-Litwa K, Asmussen H, Vicente-Manzanares M & Horwitz AR (2011) Myosin IIB Activity and Phosphorylation Status Determines Dendritic Spine and Post-Synaptic Density Morphology. *PLOS ONE* 6: e24149

Hotulainen P, Llano O, Smirnov S, Tanhuanpää K, Faix J, Rivera C & Lappalainen P (2009) Defining mechanisms of actin polymerization and depolymerization during dendritic spine morphogenesis. *J Cell Biol* 185: 323–339

941 Huehn AR, Bibeau JP, Schramm AC, Cao W, De La Cruz EM & Sindelar CV (2020) Structures of
942 cofilin-induced structural changes reveal local and asymmetric perturbations of actin filaments. *Proc*
943 *Natl Acad Sci U S A* 117
944
945 Hundt N, Preller M, Swolski O, Ang AM, Mannherz HG, Manstein DJ & Müller M (2014) Molecular
946 mechanisms of disease-related human β-actin mutations p.R183W and p.E364K. *FEBS J* 281: 5279–
947 5291
948
949 Hundt N, Steffen W, Pathan-Chhatbar S, Taft MH & Manstein DJ (2016) Load-dependent modulation
950 of non-muscle myosin-2A function by tropomyosin 4.2. *Sci Rep* 6: 20554
951
952 Ilkovski B, Nowak KJ, Domazetovska A, Maxwell AL, Clement S, Davies KE, Laing NG, North KN &
953 Cooper ST (2004) Evidence for a dominant-negative effect in ACTA1 nemaline myopathy caused by
954 abnormal folding, aggregation and altered polymerization of mutant actin isoforms. *Hum Mol Genet* 13:
955 1727–1743
956
957 Jepsen L, Kruth KA, Rubenstein PA & Sept D (2016) Two Deafness-Causing Actin Mutations
958 (DFNA20/26) Have Allosteric Effects on the Actin Structure. *Biophys J* 111
959
960 Kaindl AM, Rüschendorf F, Krause S, Goebel H-H, Koehler K, Becker C, Pongratz D, Müller-Höcker
961 J, Nürnberg P, Stoltenburg-Didinger G, *et al* (2004) Missense mutations of ACTA1 cause dominant
962 congenital myopathy with cores. *J Med Genet* 41: 842–848
963
964 Kawamoto S & Adelstein RS (1991) Chicken nonmuscle myosin heavy chains: differential expression
965 of two mRNAs and evidence for two different polypeptides. *J Cell Biol* 112: 915–924
966
967 Kron SJ & Spudich JA (1986) Fluorescent actin filaments move on myosin fixed to a glass surface. *Proc*
968 *Natl Acad Sci* 83: 6272–6276
969
970 Kruth KA & Rubenstein PA (2012) Two deafness-causing (DFNA20/26) actin mutations affect Arp2/3-
971 dependent actin regulation. *J Biol Chem* 287: 27217–27226
972
973 Kurzawa SE & Geeves MA (1996) A novel stopped-flow method for measuring the affinity of actin for
974 myosin head fragments using μg quantities of protein. *J Muscle Res Cell Motil* 17: 669–676
975
976 Laing NG, Dye DE, Wallgren-Pettersson C, Richard G, Monnier N, Lillis S, Winder TL, Lochmüller H,
977 Graziano C, Mitrani-Rosenbaum S, *et al* (2009) Mutations and polymorphisms of the skeletal muscle α-
978 actin gene (ACTA1). *Hum Mutat* 30: 1267–1277
979
980 Latham SL, Chaponnier C, Dugina V, Couraud P-O, Grau GER & Combes V (2013) Cooperation
981 between β- and γ-cytoplasmic actins in the mechanical regulation of endothelial microparticle formation.
982 *FASEB J* 27: 672–683
983
984 Latham SL, Ehmke N, Reinke PYA, Taft MH, Eicke D, Reindl T, Stenzel W, Lyons MJ, Friez MJ, Lee
985 JA, *et al* (2018) Variants in exons 5 and 6 of ACTB cause syndromic thrombocytopenia. *Nat Commun*
986 9
987
988

Lauffenburger DA & Horwitz AF (1996) Cell Migration: A Physically Integrated Molecular Process. *Cell* 84: 359–369

Lehrer SS & Kerwar G (1972) Intrinsic fluorescence of actin. *Biochemistry* 11: 1211–1217

Loisel TP, Boujemaa R, Pantaloni D & Carlier MF (1999) Reconstitution of actin-based motility of Listeria and Shigella using pure proteins. *Nature* 401: 613–616

Lu H, Fagnant PM, Bookwalter CS, Joel P & Trybus KM (2015) Vascular disease-causing mutation R258C in ACTA2 disrupts actin dynamics and interaction with myosin. *Proc Natl Acad Sci U S A* 112: E4168-4177

Ma X, Kawamoto S, Hara Y & Adelstein RS (2004) A point mutation in the motor domain of nonmuscle myosin II-B impairs migration of distinct groups of neurons. *Mol Biol Cell* 15: 2568–2579

Ma X, Uchida Y, Wei T, Liu C, Adams RH, Kubota Y, Gutkind JS, Mukouyama Y & Adelstein RS (2020) Nonmuscle myosin 2 regulates cortical stability during sprouting angiogenesis. *Mol Biol Cell* 31: 1974–1987

McCormack EA, Llorca O, Carrascosa JL, Valpuesta JM & Willison KR (2001a) Point mutations in a hinge linking the small and large domains of beta-actin result in trapped folding intermediates bound to cytosolic chaperonin CCT. *J Struct Biol* 135: 198–204

McCormack EA, Rohman MJ & Willison KR (2001b) Mutational screen identifies critical amino acid residues of β-actin mediating interaction between its folding intermediates and eukaryotic cytosolic chaperonin CCT. *J Struct Biol* 135

Micheva KD, Vallée A, Beaulieu C, Herman IM & Leclerc N (1998) beta-Actin is confined to structures having high capacity of remodelling in developing and adult rat cerebellum. *Eur J Neurosci* 10: 3785–3798

Morín M, Bryan KE, Mayo-Merino F, Goodyear R, Mencía Á, Modamio-Høybjør S, Del Castillo I, Cabalka JM, Richardson G, Moreno F, *et al* (2009) In vivo and in vitro effects of two novel gamma-actin (ACTG1) mutations that cause DFNA20/26 hearing impairment. *Hum Mol Genet* 18

Müller M, Diensthuber RP, Chizhov I, Claus P, Heissler SM, Preller M, Taft MH & Manstein DJ (2013) Distinct Functional Interactions between Actin Isoforms and Nonsarcomeric Myosins. *PLoS ONE* 8

Müller M, Mazur AJ, Behrmann E, Diensthuber RP, Radke MB, Qu Z, Littwitz C, Raunser S, Schoenenberger C-A, Manstein DJ, *et al* (2012) Functional characterization of the human α-cardiac actin mutations Y166C and M305L involved in hypertrophic cardiomyopathy. *Cell Mol Life Sci CMLS* 69: 3457–3479

Mullins RD, Heuser JA & Pollard TD (1998) The interaction of Arp2/3 complex with actin: Nucleation, high affinity pointed end capping, and formation of branching networks of filaments. *Proc Natl Acad Sci*

1037 Murakami N & Elzinga M (1992) Immunohistochemical studies on the distribution of cellular myosin
1038 II isoforms in brain and aorta. *Cell Motil* 22: 281–295
1039
1040 Namme JN, Bepari AK & Takebayashi H (2021) Cofilin Signaling in the CNS Physiology and
1041 Neurodegeneration. *Int J Mol Sci* 22: 10727
1042
1043 Ng R & Abelson J (1980) Isolation and sequence of the gene for actin in Saccharomyces cerevisiae.
1044 *Proc Natl Acad Sci U S A* 77: 3912–3916
1045
1046 Nicholson-Dykstra S, Higgs HN & Harris ES (2005) Actin Dynamics: Growth from Dendritic Branches.
1047 *Curr Biol* 15: R346–R357
1048
1049 Noguchi TQP, Kanzaki N, Ueno H, Hirose K & Uyeda TQP (2007) A novel system for expressing toxic
1050 actin mutants in Dictyostelium and purification and characterization of a dominant lethal yeast actin
1051 mutant. *J Biol Chem*
1052
1053 Noguchi TQP, Komori T, Umeki N, Demizu N, Ito K, Iwane AH, Tokuraku K, Yanagida T & Uyeda
1054 TQP (2012) G146V Mutation at the Hinge Region of Actin Reveals a Myosin Class-specific
1055 Requirement of Actin Conformations for Motility*. *J Biol Chem* 287: 24339–24345
1056
1057 Nussbaum-Krammer CI, Neto MF, Brielmann RM, Pedersen JS & Morimoto RI (2015) Investigating
1058 the spreading and toxicity of prion-like proteins using the metazoan model organism C. elegans. *J Vis*
1059 *Exp JoVE*: 52321
1060
1061 Oda T, Iwasa M, Aihara T, Maéda Y & Narita A (2009) The nature of the globular- to fibrous-actin
1062 transition. *Nature* 457
1063
1064 Parker F, Baboolal TG & Peckham M (2020) Actin mutations and their role in disease. *Int J Mol Sci* 21
1065
1066 Pathan-Chhatbar S, Taft MH, Reindl T, Hundt N, Latham SL & Manstein DJ (2018) Three mammalian
1067 tropomyosin isoforms have different regulatory effects on nonmuscle myosin-2B and filamentous β-
1068 actin in vitro. *J Biol Chem* 293: 863–875
1069
1070 Pavlyk I, Leu NA, Vedula P, Kurosaka S & Kashina A (2018) Rapid and dynamic arginylation of the
1071 leading edge β-actin is required for cell migration. *Traffic* 19
1072
1073 Pettersen EF, Goddard TD, Huang CC, Meng EC, Couch GS, Croll TI, Morris JH & Ferrin TE (2021)
1074 UCSF ChimeraX: Structure visualization for researchers, educators, and developers. *Protein Sci Publ*
1075 *Protein Soc* 30: 70–82
1076
1077 Plastino J & Blanchoin L (2019) Dynamic stability of the actin ecosystem. *J Cell Sci* 132
1078
1079 Pollard TD (2016) Actin and actin-binding proteins. *Cold Spring Harb Perspect Biol* 8
1080
1081 Pollard TD, Blanchoin L & Mullins RD (2002) Molecular Mechanisms Controlling Actin Filament
1082 Dynamics in Nonmuscle Cells. *Annu Rev Biophys Biomol Struct*
1083
1084

1085 Ponti A, Machacek M, Gupton SL, Waterman-Storer CM & Danuser G (2004) Two Distinct Actin
1086 Networks Drive the Protrusion of Migrating Cells. *Science* 305: 1782–1786
1087
1088 Pope BJ, Gonsior SM, Yeoh S, McGough A & Weeds AG (2000) Uncoupling actin filament
1089 fragmentation by cofilin from increased subunit turnover. *J Mol Biol* 298: 649–661
1090
1091 Pospich S, Sweeney HL, Houdusse A & Raunser S (2021) High-resolution structures of the actomyosin-
1092 V complex in three nucleotide states provide insights into the force generation mechanism. *eLife* 10:
1093 e73724
1094
1095 Reindl T, Giese S, Greve JN, Reinke PY, Chizhov I, Latham SL, Mulvihill DP, Taft MH & Manstein
1096 DJ (2022) Distinct actin–tropomyosin cofilament populations drive the functional diversification of
1097 cytoskeletal myosin motor complexes. *iScience* 25: 104484
1098
1099 Rendtorff NDND, Zhu M, Fagerheim T, Antal TL, Jones MP, Teslovich TM, Gillanders EM, Barmada
1100 M, Teig E, Trent JM, *et al* (2006) A novel missense mutation in ACTG1 causes dominant deafness in a
1101 Norwegian DFNA20/26 family, but ACTG1 mutations are not frequent among families with hereditary
1102 hearing impairment. *Eur J Hum Genet*
1103
1104 Rex CS, Gavin CF, Rubio MD, Kramar EA, Chen LY, Jia Y, Huganir RL, Muzyczka N, Gall CM, Miller
1105 CA, *et al* (2010) Myosin IIb regulates actin dynamics during synaptic plasticity and memory formation.
1106 *Neuron* 67: 603–617
1107
1108 Ridley AJ, Schwartz MA, Burridge K, Firtel RA, Ginsberg MH, Borisy G, Parsons JT & Horwitz AR
1109 (2003) Cell Migration: Integrating Signals from Front to Back. *Science* 302: 1704–1709
1110
1111 Risi C, Schäfer LU, Belknap B, Pepper I, White HD, Schröder GF & Galkin VE (2021) High-Resolution
1112 Cryo-EM Structure of the Cardiac Actomyosin Complex. *Structure* 29: 50-60.e4
1113
1114 Rivière JB, Van Bon BWM, Hoischen A, Kholmanskikh SS, O'Roak BJ, Gilissen C, Gijsen S, Sullivan
1115 CT, Christian SL, Abdul-Rahman OA, *et al* (2012) De novo mutations in the actin genes ACTB and
1116 ACTG1 cause Baraitser-Winter syndrome. *Nat Genet* 44: 440–444
1117
1118 Robert-Paganin J, Xu X-P, Swift MF, Auguin D, Robblee JP, Lu H, Fagnant PM, Krementsova EB,
1119 Trybus KM, Houdusse A, *et al* (2021) The actomyosin interface contains an evolutionary conserved
1120 core and an ancillary interface involved in specificity. *Nat Commun* 12: 1892
1121
1122 Rochlin MW, Itoh K, Adelstein RS & Bridgman PC (1995) Localization of myosin II A and B isoforms
1123 in cultured neurons. *J Cell Sci* 108 (Pt 12): 3661–3670
1124
1125 Rueden CT, Schindelin J, Hiner MC, DeZonia BE, Walter AE, Arena ET & Eliceiri KW (2017)
1126 ImageJ2: ImageJ for the next generation of scientific image data. *BMC Bioinformatics* 18: 529
1127
1128 Sali A & Blundell TL (1993) Comparative protein modelling by satisfaction of spatial restraints. *J Mol*
1129 *Biol* 234: 779–815
1130
1131 Savitzky Abraham & Golay MJE (1964) Smoothing and Differentiation of Data by Simplified Least
1132 Squares Procedures. *Anal Chem* 36: 1627–1639

Schröder JM, Durling H & Laing N (2004) Actin myopathy with nemaline bodies, intranuclear rods, and a heterozygous mutation in ACTA1 (Asp154Asn). *Acta Neuropathol (Berl)* 108: 250–256

Schrödinger, LLC (2015) The PyMOL Molecular Graphics System, Version 1.8.

Schüler H, Lindberg U, Schutt CE & Karlsson R (2000) Thermal unfolding of G-actin monitored with the DNase I-inhibition assay. *Eur J Biochem*

Sellers JR (2000) Myosins: a diverse superfamily. *Biochim Biophys Acta BBA - Mol Cell Res* 1496: 3–22

Star EN, Kwiatkowski DJ & Murthy VN (2002) Rapid turnover of actin in dendritic spines and its regulation by activity. *Nat Neurosci* 5: 239–246

Suhre K & Sanejouand Y-H (2004) ElNemo: a normal mode web server for protein movement analysis and the generation of templates for molecular replacement. *Nucleic Acids Res* 32: W610-614

Sweeney HL & Hammers DW (2018) Muscle Contraction. *Cold Spring Harb Perspect Biol* 10: a023200

Vang S, Corydon TJ, Børglum AD, Scott MD, Frydman J, Mogensen J, Gregersen N & Bross P (2005) Actin mutations in hypertrophic and dilated cardiomyopathy cause inefficient protein folding and perturbed filament formation. *FEBS J* 272

Vedula P, Kurosaka S, Leu NA, Wolf YI, Shabalina SA, Wang J, Sterling S, Dong DW & Kashina A (2017) Diverse functions of homologous actin isoforms are defined by their nucleotide, rather than their amino acid sequence. *eLife* 6

Verloes A, Di Donato N, Masliah-Planchon J, Jongmans M, Abdul-Raman OA, Albrecht B, Allanson J, Brunner H, Bertola D, Chassaing N, *et al* (2015) Baraitser-Winter cerebrofrontofacial syndrome: Delineation of the spectrum in 42 cases. *Eur J Hum Genet* 23: 292–301

Von Der Ecken J, Heissler SM, Pathan-Chhatbar S, Manstein DJ & Raunser S (2016) Cryo-EM structure of a human cytoplasmic actomyosin complex at near-atomic resolution. *Nature* 534: 724–728

Weinberger R, Schevzov G, Jeffrey P, Gordon K, Hill M & Gunning P (1996) The molecular composition of neuronal microfilaments is spatially and temporally regulated. *J Neurosci Off J Soc Neurosci* 16: 238–252

Whitmore L & Wallace BA (2004) DICHROWEB, an online server for protein secondary structure analyses from circular dichroism spectroscopic data. *Nucleic Acids Res* 32: W668–W673

Wiggan O, Shaw AE, DeLuca JG & Bamburg JR (2012) ADF/Cofilin Regulates Actomyosin Assembly through Competitive Inhibition of Myosin II Binding to F-Actin. *Dev Cell* 22: 530–543

van Wijk E, Krieger E, Kemperman MH, De Leenheer EMR, Huygen PLM, Cremers CWRJ, Cremers FPM & Kremer H (2003) A mutation in the gamma actin 1 (ACTG1) gene causes autosomal dominant hearing loss (DFNA20/26). *J Med Genet* 40: 879–884

1181 Wioland H, Guichard B, Senju Y, Myram S, Lappalainen P, Jégou A & Romet-Lemonne G (2017)
1182 ADF/Cofilin Accelerates Actin Dynamics by Severing Filaments and Promoting Their
1183 Depolymerization at Both Ends. *Curr Biol* 27: 1956-1967.e7
1184
1185 Wioland H, Jegou A & Romet-Lemonne G (2019) Quantitative Variations with pH of Actin
1186 Depolymerizing Factor/Cofilin's Multiple Actions on Actin Filaments. *Biochemistry* 58
1187
1188 Witjes L, Van Troys M, Verhasselt B & Ampe C (2020) Prevalence of cytoplasmic actin mutations in
1189 diffuse large B-cell lymphoma and multiple myeloma: A functional assessment based on actin three-
1190 dimensional structures. *Int J Mol Sci*
1191
1192 Yuan Y, Gao X, Huang B, Lu J, Wang G, Lin X, Qu Y & Dai P (2016) Phenotypic Heterogeneity in a
1193 DFNA20/26 family segregating a novel ACTG1 mutation. *BMC Genet*
1194
1195 Zhang F, Saha S, Shabalina SA & Kashina A (2010) Differential arginylation of actin isoforms is
1196 regulated by coding sequence-dependent degradation. *Science* 329: 1534–1537
1197
1198 Zimmet A, Van Eeuwen T, Boczkowska M, Rebowski G, Murakami K & Dominguez R (2020) Cryo-
1199 EM structure of NPF-bound human Arp2/3 complex and activation mechanism. *Sci Adv* 6: eaaz7651
1200
1201 Abercrombie M, Heaysman JEM & Pegrum SM (1971) The locomotion of fibroblasts in culture: IV.
1202 Electron microscopy of the leading lamella. *Exp Cell Res* 67: 359–367

1203 Abercrombie M, Joan E, Heaysman M & Pegrum SM (1970) The locomotion of fibroblasts in culture: II.
1204 "Ruffling". *Exp Cell Res* 60: 437–444

1205 Andrianantoandro E & Pollard TD (2006) Mechanism of Actin Filament Turnover by Severing and
1206 Nucleation at Different Concentrations of ADF/Cofilin. *Mol Cell* 24

1207 Anson M, Geeves MA, Kurzawa SE & Manstein DJ (1996) Myosin motors with artificial lever arms.
1208 *EMBO J* 15: 6069–6074

1209 Baraitser M & Winter RM (1988) Iris coloboma, ptosis, hypertelorism, and mental retardation: a new
1210 syndrome. *J Med Genet* 25: 41–43

1211 Bassell GJ, Zhang H, Byrd AL, Femino AM, Singer RH, Taneja KL, Lifshitz LM, Herman IM & Kosik KS
1212 (1998) Sorting of beta-actin mRNA and protein to neurites and growth cones in culture. *J*
1213 *Neurosci Off J Soc Neurosci* 18: 251–265

1214 Behrmann E, Müller M, Penczek PA, Mannherz HG, Manstein DJ & Raunser S (2012) Structure of the
1215 rigor actin-tropomyosin-myosin complex. *Cell* 150: 327–338

1216 Blanchoin L, Amann KJ, Higgs HN, Marchand J-B, Kaiser DA & Pollard TD (2000) Direct observation of
1217 dendritic actin filament networks nucleated by Arp2/3 complex and WASP/Scar proteins.
1218 *Nature* 404: 1007–1011

1219 Blanchoin L & Pollard TD (1999) Mechanism of interaction of Acanthamoeba actophorin (ADF/Cofilin)
1220 with actin filaments. *J Biol Chem* 274: 15538–15546

1221 Breitsprecher D, Koestler SA, Chizhov I, Nemethova M, Mueller J, Goode BL, Small JV, Rottner K & Faix
1222 J (2011) Cofilin cooperates with fascin to disassemble filopodial actin filaments. *J Cell Sci* 124:
1223 3305–3318

1224 Bryan KE & Rubenstein PA (2009) Allele-specific effects of human deafness γ-actin mutations
1225 (DFNA20/26) on the actin/cofilin interaction. *J Biol Chem* 284

1226 Bryan KE, Wen KK, Zhu M, Rendtorff ND, Feldkamp M, Tranebjaerg L, Friderici KH & Rubenstein PA
1227 (2006) Effects of human deafness γ-actin mutations (DFNA20/26) on actin function. *J Biol Chem*
1228 281

1229 Cheever TR & Ervasti JM (2013) Actin isoforms in neuronal development and function. *Int Rev Cell Mol*
1230 *Biol* 301: 157–213

1231 Cheever TR, Li B & Ervasti JM (2012) Restricted Morphological and Behavioral Abnormalities following
1232 Ablation of β-Actin in the Brain. *PLoS ONE* 7: e32970

1233 Cope MJT, Whisstock J, Rayment I & Kendrick-Jones J (1996) Conservation within the myosin motor
1234 domain: implications for structure and function. *Structure* 4: 969–987

1235 Costa CF, Rommelaere H, Waterschoot D, Sethi KK, Nowak KJ, Laing NG, Ampe C & Machesky LM (2004)
1236 Myopathy mutations in alpha-skeletal-muscle actin cause a range of molecular defects. *J Cell*
1237 *Sci* 117: 3367–3377

1238 Cuvertino S, Stuart HM, Chandler KE, Roberts NA, Armstrong R, Bernardini L, Bhaskar S, Callewaert B,
1239 Clayton-Smith J, Davalillo CH, *et al* (2017) ACTB Loss-of-Function Mutations Result in a
1240 Pleiotropic Developmental Disorder. *Am J Hum Genet*

1241 De La Cruz EM (2005) Cofilin Binding to Muscle and Non-muscle Actin Filaments: Isoform-dependent
1242 Cooperative Interactions. *J Mol Biol* 346: 557–564

1243 De La Cruz EM & Sept D (2010) The Kinetics of Cooperative Cofilin Binding Reveals Two States of the
1244 Cofilin-Actin Filament. *Biophys J* 98: 1893–1901

1245 De La Cruz EM, Wells AL, Rosenfeld SS, Ostap EM & Sweeney HL (1999) The kinetic mechanism of
1246 myosin V. *Proc Natl Acad Sci* 96: 13726–13731

1247 Di Donato N, Kuechler A, Vergano S, Heinritz W, Bodurtha J, Merchant SR, Breningstall G, Ladda R, Sell
1248 S, Altmüller J, *et al* (2016) Update on the ACTG1-associated Baraitser–Winter
1249 cerebrofrontofacial syndrome. *Am J Med Genet A* 170

1250 Di Donato N, Rump A, Koenig R, Der Kaloustian VM, Halal F, Sonntag K, Krause C, Hackmann K, Hahn
1251 G, Schrock E, *et al* (2014) Severe forms of Baraitser-Winter syndrome are caused by ACTB
1252 mutations rather than ACTG1 mutations. *Eur J Hum Genet* 22: 179–183

1253 Domingues HS, Urbanski MM, Macedo-Ribeiro S, Almaktari A, Irfan A, Hernandez Y, Wang H, Relvas JB,
1254 Rubinstein B, Melendez-Vasquez CV, *et al* (2020) Pushing myelination – developmental
1255 regulation of myosin expression drives oligodendrocyte morphological differentiation. *J Cell*
1256 *Sci* 133: jcs232264

1257 Dominguez R & Holmes KC (2011) Actin Structure and Function. *Annu Rev Biophys* 40: 169–186

1258 Doolittle LK, Rosen MK & Padrick SB (2013) Measurement and analysis of in vitro actin polymerization.
1259 *Methods Mol Biol* 1046

1260 Du J & Frieden C (1998) Kinetic Studies on the Effect of Yeast Cofilin on Yeast Actin Polymerization.
1261 *Biochemistry* 37: 13276–13284

1262 Dugina V, Khromova N, Rybko V, Blizniukov O, Shagieva G, Chaponnier C, Kopnin B & Kopnin P (2015)
1263 Tumor promotion by γ and suppression by β non-muscle actin isoforms. *Oncotarget* 6: 14556–
1264 14571

1265 Dugina V, Zwaenepoel I, Gabbiani G, Clément S & Chaponnier C (2009) Beta and gamma-cytoplasmic
1266 actins display distinct distribution and functional diversity. *J Cell Sci* 122: 2980–8

1267 Ecken J von der, Heissler SM, Pathan-Chhatbar S, Manstein DJ & Raunser S (2016a) Cryo-EM structure
1268 of a human cytoplasmic actomyosin complex at near-atomic resolution. *Nature* 534: 724–728

1269 Ecken J von der, Heissler SM, Pathan-Chhatbar S, Manstein DJ & Raunser S (2016b) Cryo-EM structure
1270 of a human cytoplasmic actomyosin complex at near-atomic resolution. *Nature* 534: 724–728

1271 Fujii T & Namba K (2017) Structure of actomyosin rigour complex at 5.2 Å resolution and insights into
1272 the ATPase cycle mechanism. *Nat Commun* 8: 13969

1273 Furch M, Geeves MA & Manstein DJ (1998) Modulation of Actin Affinity and Actomyosin Adenosine
1274 Triphosphatase by Charge Changes in the Myosin Motor Domain. *Biochemistry* 37: 6317–6326

1275 Goddard TD, Huang CC, Meng EC, Pettersen EF, Couch GS, Morris JH & Ferrin TE (2018) UCSF ChimeraX:
1276 Meeting modern challenges in visualization and analysis. *Protein Sci Publ Protein Soc* 27: 14–
1277 25

1278 Goley ED & Welch MD (2006) The ARP2/3 complex: an actin nucleator comes of age. *Nat Rev Mol Cell*
1279 *Biol* 7: 713–726

1280 Golomb E, Ma X, Jana SS, Preston YA, Kawamoto S, Shoham NG, Goldin E, Conti MA, Sellers JR &
1281 Adelstein RS (2004) Identification and characterization of nonmuscle myosin II-C, a new
1282 member of the myosin II family. *J Biol Chem* 279: 2800–2808

1283 Gong R, Jiang F, Moreland ZG, Reynolds MJ, de los Reyes SE, Gurel P, Shams A, Heidings JB, Bowl MR,
1284 Bird JE, *et al* (2022) Structural basis for tunable control of actin dynamics by myosin-15 in
1285 mechanosensory stereocilia. *Sci Adv* 8: eabl4733

1286 Greve JN, Schwäbe FV, Pokrant T, Faix J, Di Donato N, Taft MH & Manstein DJ (2022) Frameshift
1287 mutation S368fs in the gene encoding cytoskeletal β-actin leads to ACTB-associated syndromic
1288 thrombocytopenia by impairing actin dynamics. *Eur J Cell Biol* 101: 151216

1289 Gurel PS, Kim LY, Ruijgrok PV, Omabegho T, Bryant Z & Alushin GM (2017) Cryo-EM structures reveal
1290 specialization at the myosin VI-actin interface and a mechanism of force sensitivity. *eLife* 6:
1291 e31125

1292 Gyimesi M, Horváth ÁI, Túrós D, Suthar SK, Pénzes M, Kurdi C, Canon L, Kikuti C, Ruppel KM, Trivedi
1293 DV, *et al* (2020) Single Residue Variation in Skeletal Muscle Myosin Enables Direct and Selective
1294 Drug Targeting for Spasticity and Muscle Stiffness. *Cell* 183: 335-346.e13

1295 Hammer JA & Wagner W (2013) Functions of Class V Myosins in Neurons. *J Biol Chem* 288: 28428–
1296 28434

1297 Heissler SM & Manstein DJ (2011) Comparative kinetic and functional characterization of the motor
1298 domains of human nonmuscle myosin-2C isoforms. *J Biol Chem* 286: 21191–21202

1299 Hodges JL, Newell-Litwa K, Asmussen H, Vicente-Manzanares M & Horwitz AR (2011) Myosin IIB
1300 Activity and Phosphorylation Status Determines Dendritic Spine and Post-Synaptic Density
1301 Morphology. *PLOS ONE* 6: e24149

1302 Hotulainen P, Llano O, Smirnov S, Tanhuanpää K, Faix J, Rivera C & Lappalainen P (2009) Defining
1303 mechanisms of actin polymerization and depolymerization during dendritic spine
1304 morphogenesis. *J Cell Biol* 185: 323–339

1305 Hundt N, Preller M, Swolski O, Ang AM, Mannherz HG, Manstein DJ & Müller M (2014) Molecular
1306 mechanisms of disease-related human β-actin mutations p.R183W and p.E364K. *FEBS J* 281:
1307 5279–5291

1308 Hundt N, Steffen W, Pathan-Chhatbar S, Taft MH & Manstein DJ (2016) Load-dependent modulation
1309 of non-muscle myosin-2A function by tropomyosin 4.2. *Sci Rep* 6: 20554

1310 Ilkovski B, Nowak KJ, Domazetovska A, Maxwell AL, Clement S, Davies KE, Laing NG, North KN & Cooper
1311 ST (2004) Evidence for a dominant-negative effect in ACTA1 nemaline myopathy caused by
1312 abnormal folding, aggregation and altered polymerization of mutant actin isoforms. *Hum Mol*
1313 *Genet* 13: 1727–1743

1314 Jepsen L, Kruth KA, Rubenstein PA & Sept D (2016) Two Deafness-Causing Actin Mutations
1315 (DFNA20/26) Have Allosteric Effects on the Actin Structure. *Biophys J* 111

1316 Kaindl AM, Rüschendorf F, Krause S, Goebel H-H, Koehler K, Becker C, Pongratz D, Müller-Höcker J,
1317 Nürnberg P, Stoltenburg-Didinger G, *et al* (2004) Missense mutations of ACTA1 cause dominant
1318 congenital myopathy with cores. *J Med Genet* 41: 842–848

1319 Kawamoto S & Adelstein RS (1991) Chicken nonmuscle myosin heavy chains: differential expression of
1320 two mRNAs and evidence for two different polypeptides. *J Cell Biol* 112: 915–924

1321 Kron SJ & Spudich JA (1986) Fluorescent actin filaments move on myosin fixed to a glass surface. *Proc*
1322 *Natl Acad Sci* 83: 6272–6276

1323 Kruth KA & Rubenstein PA (2012) Two deafness-causing (DFNA20/26) actin mutations affect Arp2/3-
1324 dependent actin regulation. *J Biol Chem* 287: 27217–27226

1325 Kurzawa SE & Geeves MA (1996) A novel stopped-flow method for measuring the affinity of actin for
1326 myosin head fragments using µg quantities of protein. *J Muscle Res Cell Motil* 17: 669–676

1327 Laing NG, Dye DE, Wallgren-Pettersson C, Richard G, Monnier N, Lillis S, Winder TL, Lochmüller H,
1328 Graziano C, Mitrani-Rosenbaum S, *et al* (2009) Mutations and polymorphisms of the skeletal
1329 muscle α-actin gene (ACTA1). *Hum Mutat* 30: 1267–1277

1330 Latham SL, Chaponnier C, Dugina V, Couraud P-O, Grau GER & Combes V (2013) Cooperation between
1331 β- and γ-cytoplasmic actins in the mechanical regulation of endothelial microparticle
1332 formation. *FASEB J* 27: 672–683

1333 Latham SL, Ehmke N, Reinke PYA, Taft MH, Eicke D, Reindl T, Stenzel W, Lyons MJ, Friez MJ, Lee JA, *et*
1334 *al* (2018) Variants in exons 5 and 6 of ACTB cause syndromic thrombocytopenia. *Nat Commun*
1335 9

1336 Lauffenburger DA & Horwitz AF (1996) Cell Migration: A Physically Integrated Molecular Process. *Cell*
1337 84: 359–369

1338 Lehrer SS & Kerwar G (1972) Intrinsic fluorescence of actin. *Biochemistry* 11: 1211–1217

1339 Lobley A, Whitmore L & Wallace BA (2002) DICHROWEB: an interactive website for the analysis of
1340 protein secondary structure from circular dichroism spectra. *Bioinforma Oxf Engl* 18: 211–212

1341 Loisel TP, Boujemaa R, Pantaloni D & Carlier MF (1999) Reconstitution of actin-based motility of Listeria
1342 and Shigella using pure proteins. *Nature* 401: 613–616

1343 Lu H, Fagnant PM, Bookwalter CS, Joel P & Trybus KM (2015) Vascular disease-causing mutation R258C
1344 in ACTA2 disrupts actin dynamics and interaction with myosin. *Proc Natl Acad Sci U S A* 112:
1345 E4168-4177

1346 Ma X, Kawamoto S, Hara Y & Adelstein RS (2004) A point mutation in the motor domain of nonmuscle
1347 myosin II-B impairs migration of distinct groups of neurons. *Mol Biol Cell* 15: 2568–2579

1348 Ma X, Uchida Y, Wei T, Liu C, Adams RH, Kubota Y, Gutkind JS, Mukouyama Y & Adelstein RS (2020)
1349 Nonmuscle myosin 2 regulates cortical stability during sprouting angiogenesis. *Mol Biol Cell* 31:
1350 1974–1987

1351 McCormack EA, Llorca O, Carrascosa JL, Valpuesta JM & Willison KR (2001a) Point mutations in a hinge
1352 linking the small and large domains of beta-actin result in trapped folding intermediates bound
1353 to cytosolic chaperonin CCT. *J Struct Biol* 135: 198–204

1354 McCormack EA, Rohman MJ & Willison KR (2001b) Mutational screen identifies critical amino acid
1355 residues of β-actin mediating interaction between its folding intermediates and eukaryotic
1356 cytosolic chaperonin CCT. *J Struct Biol* 135

1357 Micheva KD, Vallée A, Beaulieu C, Herman IM & Leclerc N (1998) beta-Actin is confined to structures
1358 having high capacity of remodelling in developing and adult rat cerebellum. *Eur J Neurosci* 10:
1359 3785–3798

1360 Morín M, Bryan KE, Mayo-Merino F, Goodyear R, Mencía Á, Modamio-Høybjør S, Del Castillo I, Cabalka
1361 JM, Richardson G, Moreno F, *et al* (2009) In vivo and in vitro effects of two novel gamma-actin
1362 (ACTG1) mutations that cause DFNA20/26 hearing impairment. *Hum Mol Genet* 18

1363 Müller M, Diensthuber RP, Chizhov I, Claus P, Heissler SM, Preller M, Taft MH & Manstein DJ (2013)
1364 Distinct Functional Interactions between Actin Isoforms and Nonsarcomeric Myosins. *PLoS*
1365 *ONE* 8

1366 Müller M, Mazur AJ, Behrmann E, Diensthuber RP, Radke MB, Qu Z, Littwitz C, Raunser S,
1367 Schoenenberger C-A, Manstein DJ, *et al* (2012) Functional characterization of the human α-
1368 cardiac actin mutations Y166C and M305L involved in hypertrophic cardiomyopathy. *Cell Mol*
1369 *Life Sci CMLS* 69: 3457–3479

1370 Mullins RD, Heuser JA & Pollard TD (1998) The interaction of Arp2/3 complex with actin: Nucleation,
1371 high affinity pointed end capping, and formation of branching networks of filaments. *Proc Natl*
1372 *Acad Sci*

1373 Murakami N & Elzinga M (1992) Immunohistochemical studies on the distribution of cellular myosin II
1374 isoforms in brain and aorta. *Cell Motil* 22: 281–295

1375 Namme JN, Bepari AK & Takebayashi H (2021) Cofilin Signaling in the CNS Physiology and
1376 Neurodegeneration. *Int J Mol Sci* 22: 10727

1377 Ng R & Abelson J (1980) Isolation and sequence of the gene for actin in Saccharomyces cerevisiae. *Proc*
1378 *Natl Acad Sci U S A* 77: 3912–3916

1379 Nicholson-Dykstra S, Higgs HN & Harris ES (2005) Actin Dynamics: Growth from Dendritic Branches.
1380 *Curr Biol* 15: R346–R357

1381 Noguchi TQP, Kanzaki N, Ueno H, Hirose K & Uyeda TQP (2007) A novel system for expressing toxic
1382 actin mutants in Dictyostelium and purification and characterization of a dominant lethal yeast
1383 actin mutant. *J Biol Chem*

1384 Noguchi TQP, Komori T, Umeki N, Demizu N, Ito K, Iwane AH, Tokuraku K, Yanagida T & Uyeda TQP
1385 (2012) G146V Mutation at the Hinge Region of Actin Reveals a Myosin Class-specific
1386 Requirement of Actin Conformations for Motility*. *J Biol Chem* 287: 24339–24345

1387 Nussbaum-Krammer CI, Neto MF, Brielmann RM, Pedersen JS & Morimoto RI (2015) Investigating the
1388 spreading and toxicity of prion-like proteins using the metazoan model organism C. elegans. *J*
1389 *Vis Exp JoVE*: 52321

1390 Oda T, Iwasa M, Aihara T, Maéda Y & Narita A (2009) The nature of the globular- to fibrous-actin
1391 transition. *Nature* 457

1392 Parker F, Baboolal TG & Peckham M (2020) Actin mutations and their role in disease. *Int J Mol Sci* 21

1393 Pathan-Chhatbar S, Taft MH, Reindl T, Hundt N, Latham SL & Manstein DJ (2018) Three mammalian
1394 tropomyosin isoforms have different regulatory effects on nonmuscle myosin-2B and
1395 filamentous β-actin in vitro. *J Biol Chem* 293: 863–875

1396 Pettersen EF, Goddard TD, Huang CC, Meng EC, Couch GS, Croll TI, Morris JH & Ferrin TE (2021) UCSF
1397 ChimeraX: Structure visualization for researchers, educators, and developers. *Protein Sci Publ*
1398 *Protein Soc* 30: 70–82

1399 Plastino J & Blanchoin L (2019) Dynamic stability of the actin ecosystem. *J Cell Sci* 132

1400 Pollard TD (2016) Actin and actin-binding proteins. *Cold Spring Harb Perspect Biol* 8

1401 Pollard TD, Blanchoin L & Mullins RD (2002) Molecular Mechanisms Controlling Actin Filament
1402 Dynamics in Nonmuscle Cells. *Annu Rev Biophys Biomol Struct*

1403 Ponti A, Machacek M, Gupton SL, Waterman-Storer CM & Danuser G (2004) Two Distinct Actin
1404 Networks Drive the Protrusion of Migrating Cells. *Science* 305: 1782–1786

1405 Pope BJ, Gonsior SM, Yeoh S, McGough A & Weeds AG (2000) Uncoupling actin filament fragmentation
1406 by cofilin from increased subunit turnover. *J Mol Biol* 298: 649–661

1407 Pospich S, Sweeney HL, Houdusse A & Raunser S (2021) High-resolution structures of the actomyosin-
1408 V complex in three nucleotide states provide insights into the force generation mechanism.
1409 *eLife* 10: e73724

1410 Reindl T, Giese S, Greve JN, Reinke PY, Chizhov I, Latham SL, Mulvihill DP, Taft MH & Manstein DJ (2022)
1411 Distinct actin–tropomyosin cofilament populations drive the functional diversification of
1412 cytoskeletal myosin motor complexes. *iScience* 25: 104484

1413 Rendtorff NDND, Zhu M, Fagerheim T, Antal TL, Jones MP, Teslovich TM, Gillanders EM, Barmada M,
1414 Teig E, Trent JM, *et al* (2006) A novel missense mutation in ACTG1 causes dominant deafness

in a Norwegian DFNA20/26 family, but ACTG1 mutations are not frequent among families with hereditary hearing impairment. *Eur J Hum Genet*

Rex CS, Gavin CF, Rubio MD, Kramar EA, Chen LY, Jia Y, Huganir RL, Muzyczka N, Gall CM, Miller CA, *et al* (2010) Myosin IIb regulates actin dynamics during synaptic plasticity and memory formation. *Neuron* 67: 603–617

Ridley AJ, Schwartz MA, Burridge K, Firtel RA, Ginsberg MH, Borisy G, Parsons JT & Horwitz AR (2003) Cell Migration: Integrating Signals from Front to Back. *Science* 302: 1704–1709

Risi C, Schäfer LU, Belknap B, Pepper I, White HD, Schröder GF & Galkin VE (2021) High-Resolution Cryo-EM Structure of the Cardiac Actomyosin Complex. *Structure* 29: 50-60.e4

Rivière JB, Van Bon BWM, Hoischen A, Kholmanskikh SS, O'Roak BJ, Gilissen C, Gijsen S, Sullivan CT, Christian SL, Abdul-Rahman OA, *et al* (2012) De novo mutations in the actin genes ACTB and ACTG1 cause Baraitser-Winter syndrome. *Nat Genet* 44: 440–444

Robert-Paganin J, Xu X-P, Swift MF, Auguin D, Robblee JP, Lu H, Fagnant PM, Krementsova EB, Trybus KM, Houdusse A, *et al* (2021) The actomyosin interface contains an evolutionary conserved core and an ancillary interface involved in specificity. *Nat Commun* 12: 1892

Rochlin MW, Itoh K, Adelstein RS & Bridgman PC (1995) Localization of myosin II A and B isoforms in cultured neurons. *J Cell Sci* 108 (Pt 12): 3661–3670

Rueden CT, Schindelin J, Hiner MC, DeZonia BE, Walter AE, Arena ET & Eliceiri KW (2017) ImageJ2: ImageJ for the next generation of scientific image data. *BMC Bioinformatics* 18: 529

Sali A & Blundell TL (1993) Comparative protein modelling by satisfaction of spatial restraints. *J Mol Biol* 234: 779–815

Savitzky Abraham & Golay MJE (1964) Smoothing and Differentiation of Data by Simplified Least Squares Procedures. *Anal Chem* 36: 1627–1639

Schröder JM, Durling H & Laing N (2004) Actin myopathy with nemaline bodies, intranuclear rods, and a heterozygous mutation in ACTA1 (Asp154Asn). *Acta Neuropathol (Berl)* 108: 250–256

Schrödinger, LLC (2015) The PyMOL Molecular Graphics System, Version 1.8.

Schüler H, Lindberg U, Schutt CE & Karlsson R (2000) Thermal unfolding of G-actin monitored with the DNase I-inhibition assay. *Eur J Biochem*

Sellers JR (2000) Myosins: a diverse superfamily. *Biochim Biophys Acta BBA - Mol Cell Res* 1496: 3–22

Star EN, Kwiatkowski DJ & Murthy VN (2002) Rapid turnover of actin in dendritic spines and its regulation by activity. *Nat Neurosci* 5: 239–246

Suhre K & Sanejouand Y-H (2004) ElNemo: a normal mode web server for protein movement analysis and the generation of templates for molecular replacement. *Nucleic Acids Res* 32: W610-614

Sweeney HL & Hammers DW (2018) Muscle Contraction. *Cold Spring Harb Perspect Biol* 10: a023200

Vang S, Corydon TJ, Børglum AD, Scott MD, Frydman J, Mogensen J, Gregersen N & Bross P (2005) Actin mutations in hypertrophic and dilated cardiomyopathy cause inefficient protein folding and perturbed filament formation. *FEBS J* 272

1452 Verloes A, Di Donato N, Masliah-Planchon J, Jongmans M, Abdul-Raman OA, Albrecht B, Allanson J,
1453 Brunner H, Bertola D, Chassaing N, *et al* (2015) Baraitser-Winter cerebrofrontofacial syndrome:
1454 Delineation of the spectrum in 42 cases. *Eur J Hum Genet* 23: 292–301

1455 Weinberger R, Schevzov G, Jeffrey P, Gordon K, Hill M & Gunning P (1996) The molecular composition
1456 of neuronal microfilaments is spatially and temporally regulated. *J Neurosci Off J Soc Neurosci*
1457 16: 238–252

1458 Wiggan O, Shaw AE, DeLuca JG & Bamburg JR (2012) ADF/Cofilin Regulates Actomyosin Assembly
1459 through Competitive Inhibition of Myosin II Binding to F-Actin. *Dev Cell* 22: 530–543

1460 van Wijk E, Krieger E, Kemperman MH, De Leenheer EMR, Huygen PLM, Cremers CWRJ, Cremers FPM
1461 & Kremer H (2003) A mutation in the gamma actin 1 (ACTG1) gene causes autosomal dominant
1462 hearing loss (DFNA20/26). *J Med Genet* 40: 879–884

1463 Wioland H, Guichard B, Senju Y, Myram S, Lappalainen P, Jégou A & Romet-Lemonne G (2017)
1464 ADF/Cofilin Accelerates Actin Dynamics by Severing Filaments and Promoting Their
1465 Depolymerization at Both Ends. *Curr Biol* 27: 1956-1967.e7

1466 Wioland H, Jegou A & Romet-Lemonne G (2019) Quantitative Variations with pH of Actin
1467 Depolymerizing Factor/Cofilin's Multiple Actions on Actin Filaments. *Biochemistry* 58

1468 Witjes L, Van Troys M, Verhasselt B & Ampe C (2020) Prevalence of cytoplasmic actin mutations in
1469 diffuse large B-cell lymphoma and multiple myeloma: A functional assessment based on actin
1470 three-dimensional structures. *Int J Mol Sci*

1471 Yuan Y, Gao X, Huang B, Lu J, Wang G, Lin X, Qu Y & Dai P (2016) Phenotypic Heterogeneity in a
1472 DFNA20/26 family segregating a novel ACTG1 mutation. *BMC Genet*

1473 Zimmet A, Van Eeuwen T, Boczkowska M, Rebowski G, Murakami K & Dominguez R (2020) Cryo-EM
1474 structure of NPF-bound human Arp2/3 complex and activation mechanism. *Sci Adv* 6:
1475 eaaz7651

1476

1477 # Tables

1478 **Table 1 Comparison of biochemical parameters, velocities, rate and equilibrium constants**
1479 **measured in experiments with human cytoskeletal γ–actin and variant p.E334Q.**

Parameter	γ–actin	p.E334Q	1:1 Mixture
IC_{50} (DNase–Inhibition) [nM]	22.7 ± 0.7	25.7 ± 0.6 **(* 1.1–fold ↑)**	–
T_M (Mg^{2+}–ATP–G–actin) [°C]	56.77 ± 0.24	56.19 ± 0.30 **(ns)**	–
T_M (F–actin) [°C]	65.00 ± 0.76	64.83 ± 0.25 **(ns)**	–
k_{-T} (Mg^{2+}–ε–ATP) [s^{-1}]	0.0473 ± 0.0013	0.0972 ± 0.0019 **(**** 2.1–fold ↑)**	–
k_{-D} (Mg^{2+}–ε–ADP) [s^{-1}]	0.2155 ± 0.0017	0.3199 ± 0.0027 **(**** 1.5–fold ↑)**	–
F–actin ATPase [s^{-1}]	0.00089 ± 0.00005	0.00088 ± 0.00004 **(ns)**	–
Bulk–polymerisation rate k_{obs} (pyrene) [s^{-1}]	0.0140 ± 0.0004	0.0129 ± 0.0008 **(*** 1.1–fold ↓)**	0.0134 ± 0.0006 **(* 1.04–fold ↓)**
Bulk–polymerisation rate k_{obs} (pyrene) + 10 nM Arp2/3 [s^{-1}]	0.6441 ± 0.0163	0.5458 ± 0.02256 **(** 1.2–fold ↓)**	0.6162 ± 0.0776 **(ns)**
Apparent rate of filament elongation (TIRF–M) [nm/s]	12.6 ± 0.3	11.1 ± 0.3 **(**** 1.1–fold ↓)**	–
Rate of filament disassembly k_{obs} (pyrene–actin) [s^{-1}]	0.0022 ± 0.0002	0.0029 ± 0.0003 **(**** 1.3–fold ↑)**	0.0023 ± 0.0002 **(ns)**
Rate of filament disassembly k_{obs} (pyrene–actin) + 40 nM cofilin [s^{-1}]	0.0163 ± 0.0028	0.0059 ± 0.0008 **(*** 2.8–fold ↓)**	0.0084 ± 0.0018 **(** 1.9–fold ↓)**
Sliding velocity on NM2A–HMM [nm/s]	195.3 ± 5.0	39.1 ± 3.2 **(**** 5.0–fold ↓)**	131.2 ± 10.0 **(*** 1.5–fold ↓)**
Sliding velocity on Myo5A–HMM at optimal myosin density [nm/s]	315.1 ± 28.9	190.4 ± 46.9 **(**** 1.7–fold ↓)**	–
k_{-A} (NM2A–2R) [s^{-1}]	$8.0\times10^{-5} \pm 3.3\times10^{-6}$	$4.5\times10^{-4} \pm 6.7\times10^{-6}$ **(**** 5.6–fold ↑)**	$2.3\times10^{-4} \pm 1.3\times10^{-5}$ **(*** 2.9–fold ↑)**
k_{-A}(NM2C-2R) [s^{-1}]	$3.1\times10^{-4} \pm 5.0\times10^{-6}$	$1.7\times10^{-3} \pm 5.8\times10^{-5}$ **(*** 5.6–fold ↑)**	$6.7\times10^{-4} \pm 1.5\times10^{-5}$ **(*** 2.2–fold ↑)**
K_A (NM2A–2R) [nM]	1.7 ± 0.3	16.9 ± 0.3 **(** 9.9–fold ↑)**	–
K_{DA}(NM2A–2R) [nM]	122.6 ± 11.4	353.0 ± 20.6 **(** 2.9–fold ↑)**	–
Coupling (K_{DA}/ K_A) (NM2A-2R)	72.1	20.9 **(**** 3.5–fold ↓)**	–
$1/K_1$ (NM2A–2R) [µM]	812.1 ± 82.7	863.8 ± 91.6 **(ns)**	–

1480

1481

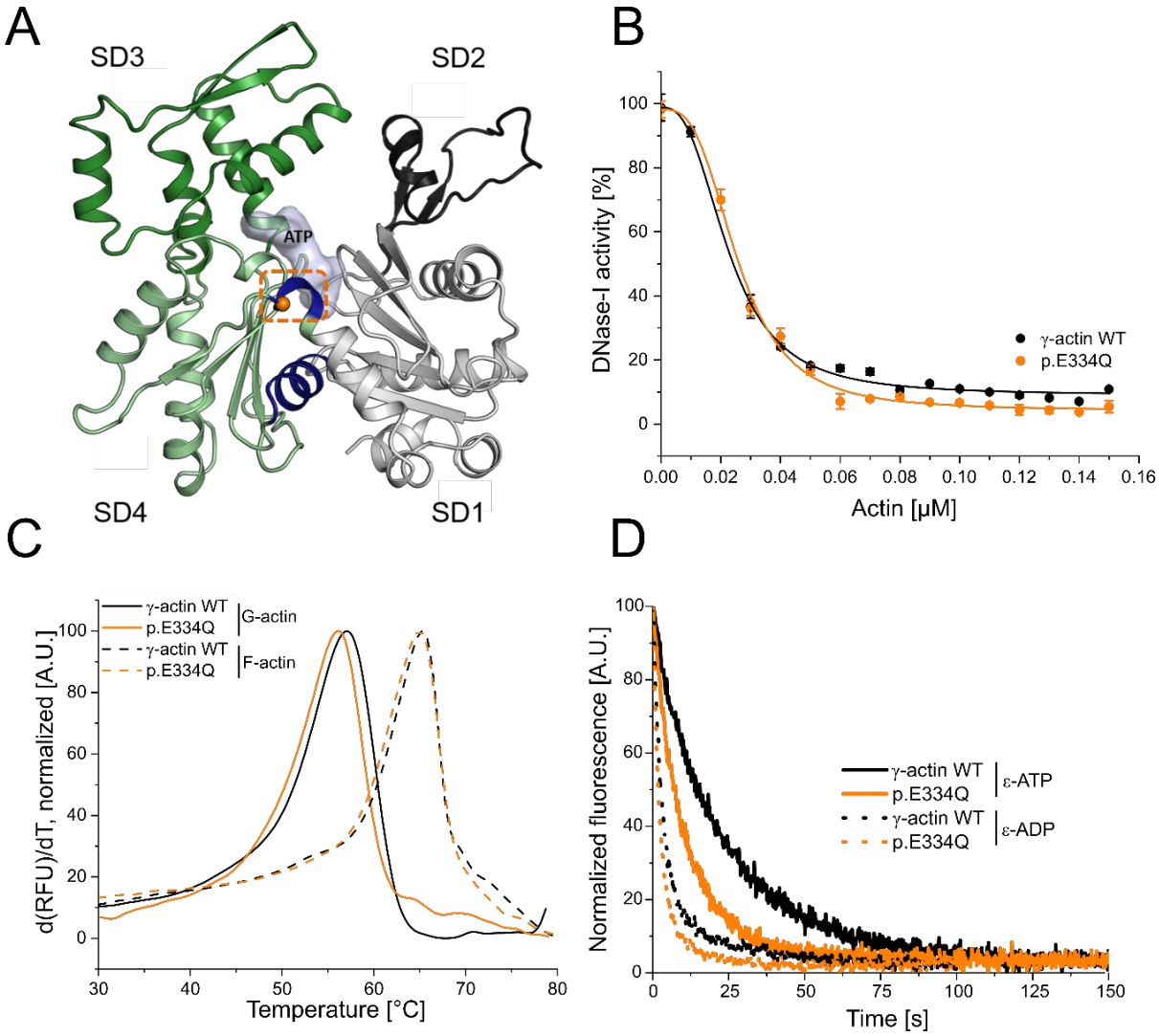

Figure 1 Analysis of actin folding, thermal stability and nucleotide exchange (A) Homology model of human cytoskeletal γ–actin (based on PDB–ID: 2BTF). Subdomains (SDs) of actin are colored in grey (SD1), dark grey (SD2), light green (SD3) and green (SD4). The hinge region encompassing residues 137–145 and 333–338 is colored in blue. The mutant residue E334 is shown as an orange sphere. **(B)** Inhibition of DNase–I activity by monomeric γ–actin WT and p.E334Q. Data is the mean of three individual experiments ± SEM. A Hill equation was fitted to the data, which yields the half–maximal inhibitory concentration (IC_{50}, Table 1). **(C)** The protein denaturation temperature of monomeric and filamentous p.E334Q and WT actin were determined by DSF. Representative experimental traces are shown. The protein denaturation temperature is derived from the peak of the melting curve (Table 1) (p.E334Q (G-actin), N=3; WT (G-actin), N=5; p.E334Q (F–actin), N=5; WT (F–actin), N=5). **(D)** Nucleotide exchange rates (k_{-T}, k_{-D}) were determined for monomeric p.E334Q and γ–actin WT using fluorescently labeled ATP (ε–ATP) (p.E334Q, N=18; WT, N=21) and ADP (ε–ADP) (p.E334Q, N=11; WT, N=11) Representative experimental traces are shown. Rates were determined by fitting a single exponential function to the data (Table 1).

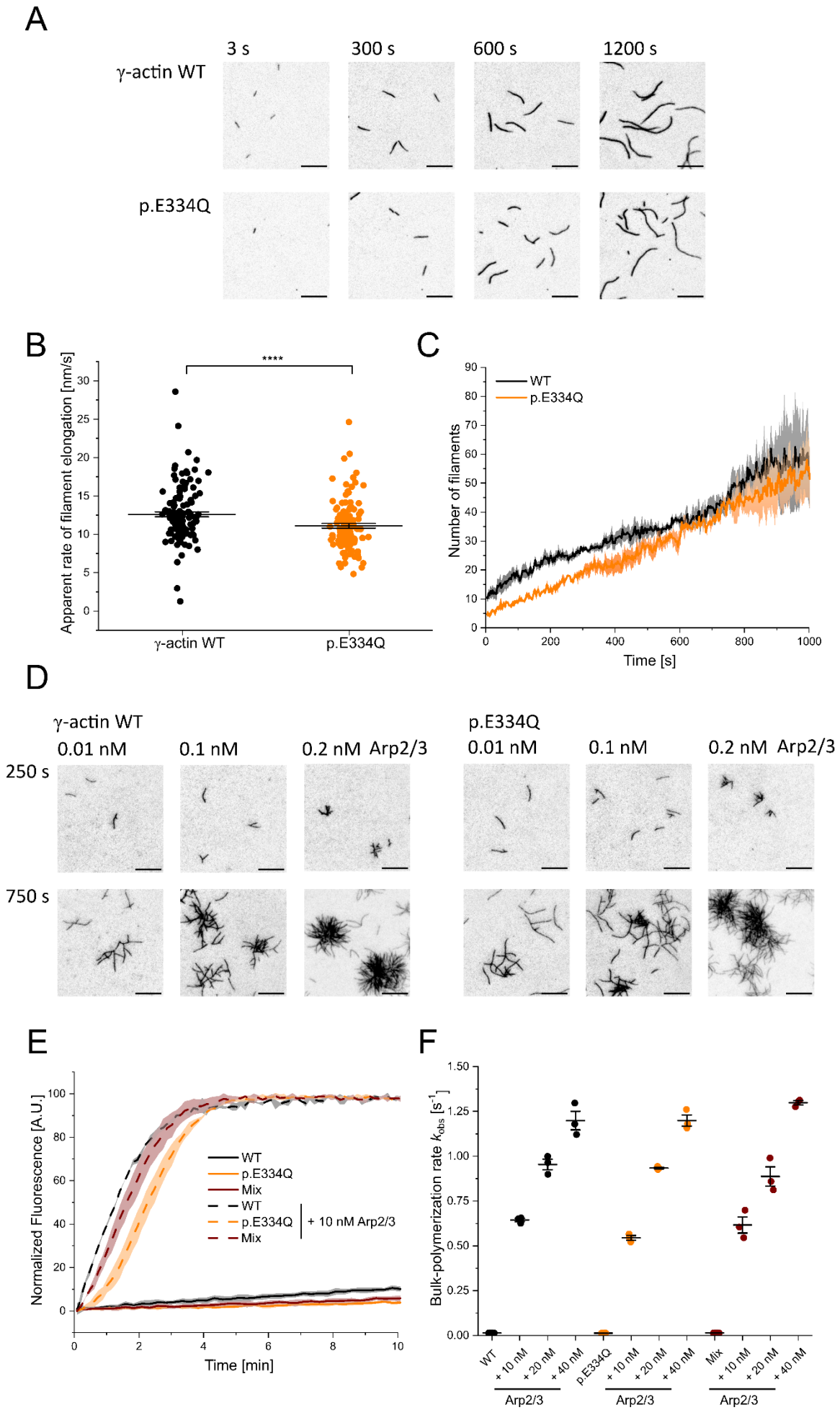
A
3 s
300 s
600 s
1200 s
γ-actin WT
p.E334Q
B
Apparent rate of filament elongation [nm/s]
****
γ-actin WT
p.E334Q
C
Number of filaments
Time [s]
WT
p.E334Q
D
γ-actin WT
0.01 nM
0.1 nM
0.2 nM Arp2/3
p.E334Q
0.01 nM
0.1 nM
0.2 nM Arp2/3
250 s
750 s
E
Normalized Fluorescence [A.U.]
Time [min]
WT
p.E334Q
Mix
WT
p.E334Q
Mix
+ 10 nM Arp2/3
F
Bulk-polymerization rate k_{obs} [s^{-1}]
WT
+ 10 nM
+ 20 nM
+ 40 nM
p.E334Q
+ 10 nM
+ 20 nM
+ 40 nM
Mix
+ 10 nM
+ 20 nM
+ 40 nM
Arp2/3
Arp2/3
Arp2/3

1500 **Figure 2 Analysis of the polymerization capacity of WT and p.E334Q γ–actin in the absence and**
1501 **presence of human Arp2/3 complex. (A)** Polymerization of p.E334Q and WT γ–actin (1 µM, 10% Atto–
1502 655 labeled) was induced by salt–shift and the progression of the reaction was tracked by TIRF
1503 microscopy. Shown are representative micrographs at the indicated points in time. Scale bar
1504 corresponds to 10 µm. **(B)** The elongation rates of individual filaments were determined by manual
1505 tracking of the elongating barbed ends of the filaments. Every data point represents an individual
1506 filament (WT: n = 128 filaments, p.E334Q: n = 114 filaments). Data is shown as the mean ± SEM from
1507 4 individual experiments. **(C)** Nucleation efficiencies were determined by monitoring changes in the
1508 number of filaments over the time of the polymerization experiments. The solid lines and shades
1509 represent the mean ± SEM of four individual experiments. **(D)** TIRF microscopy–based observation of
1510 human Arp2/3 complex mediated differences in the salt-induced polymerization of p.E334Q and WT
1511 γ–actin (1 µM, 10% Atto–655 labeled). Shown are representative micrographs at the indicated points
1512 in time. For both WT and p.E334Q γ–actin, the formation of the first branch points was observed after
1513 250 s in the presence of 0.01 nM Arp2/3. Scale bar corresponds to 10 µm. N=3 for each Arp2/3
1514 concentration **(E)** Pyrene–based polymerization experiment of 2 µM γ–actin WT, p.E334Q actin, or a
1515 1:1 mixture of both (5% pyrene–labeled) in the absence and presence of Arp2/3. Shown are
1516 representative traces. The solid lines/shades represent the mean ± SEM of at least three individual
1517 experiments. **(F)** Bulk–polymerization rates determined from the experiments shown in (E). Every data
1518 point corresponds to an individual polymerization experiment, as shown in (E). Data is shown as the
1519 mean ± SEM. Individual values and differences with statistical significance are summarized in Table 1.

1520

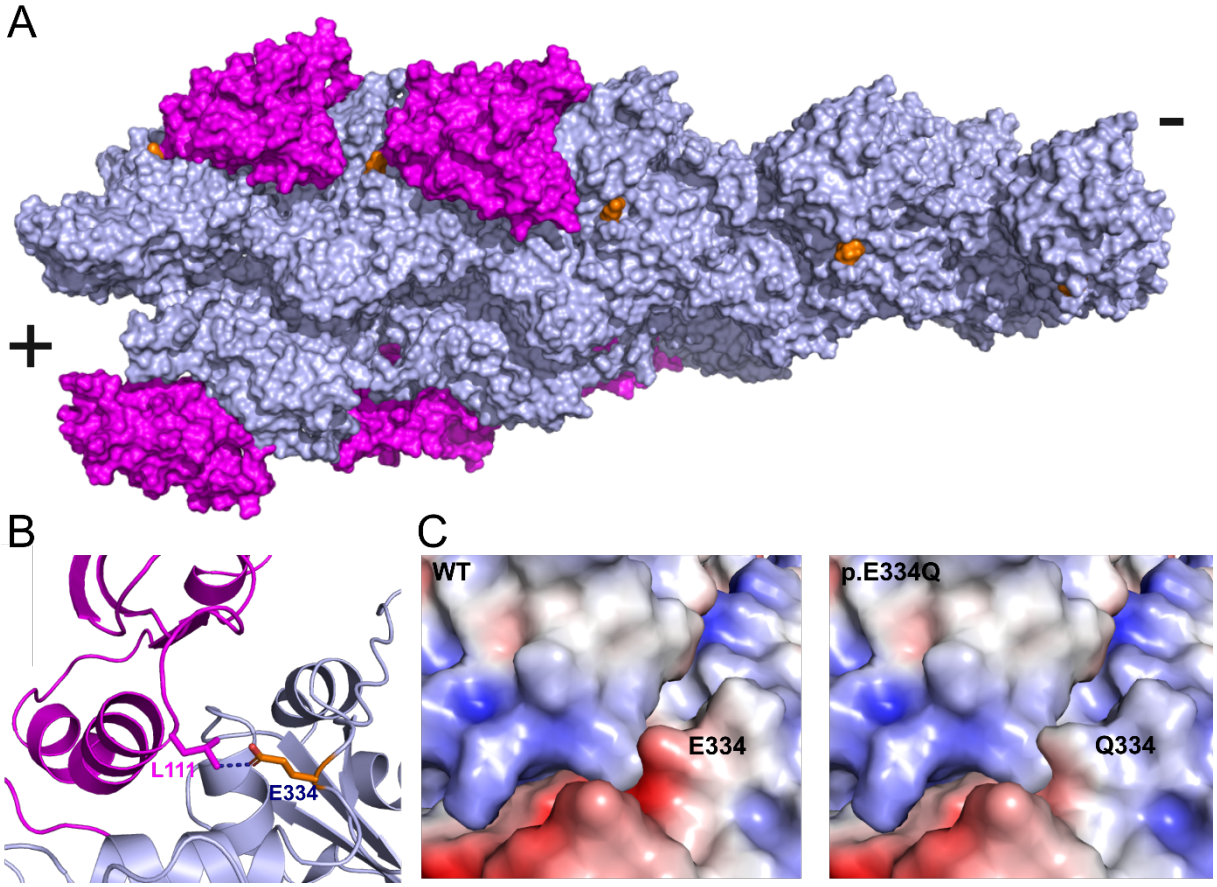

Figure 3 *In silico* analysis of the effects of the E334Q mutation on the actin–cofilin interaction. (A) Human homology model of a cytoskeletal γ–actin filament partially decorated with cofilin–1 (model based on PDB–ID:6UC4). Cofilin–1 is colored magenta, actin monomers are depicted in light blue and the actin residue E334 is colored orange. **(B)** Close up showing the details of the Van der Waals interaction between E334 and cofilin residue L111 on the pointed end side. The length of the dotted line between the side chains of actin-E334 and cofilin-L111 corresponds to 3.1 Å in our model. **(C)** The change in surface charge at the actin-cofilin interaction interface introduced by mutation E334Q is visualized by coulombic surface coloring.

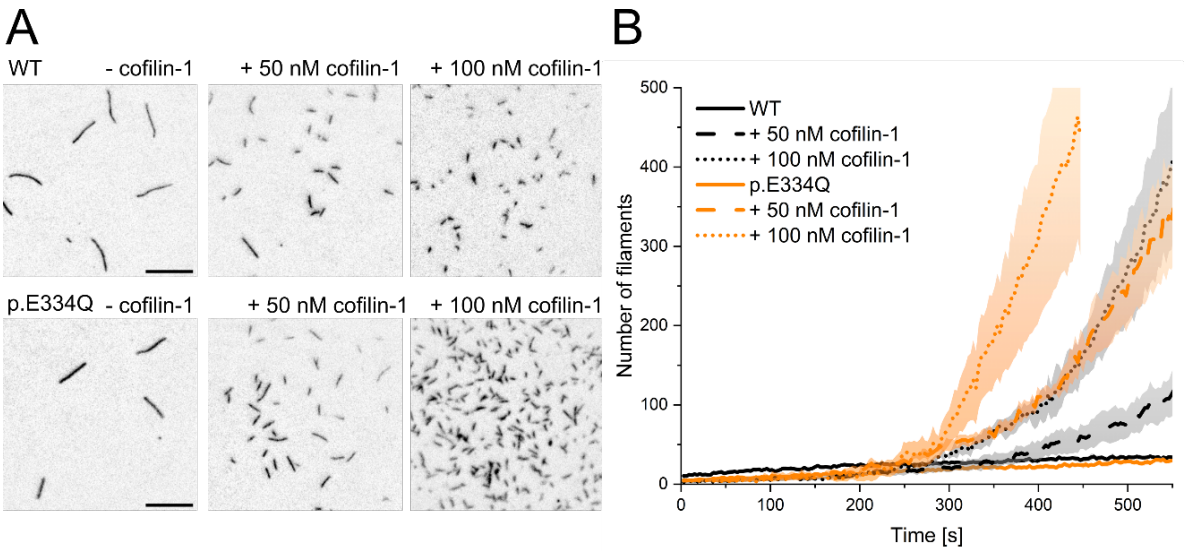

1534 **Figure 4 Analysis of the effect of cofilin–1 on the spontaneous polymerization of WT and p.E334Q γ–**
1535 **actin. (A)** TIRF microscopy–based observation of cofilin–1 mediated differences in the salt-induced
1536 polymerization of p.E334Q and WT γ–actin (1 µM, 10% Atto–655 labeled). Shown are representative
1537 micrographs 450 s after induction of polymerization. Scale bar corresponds to 10 µm. **(B)** Time
1538 dependence of the increase in filaments observed by TIRF microscopy. The solid and dotted lines and
1539 shades represent the mean ± SEM of 3 individual experiments.

1540

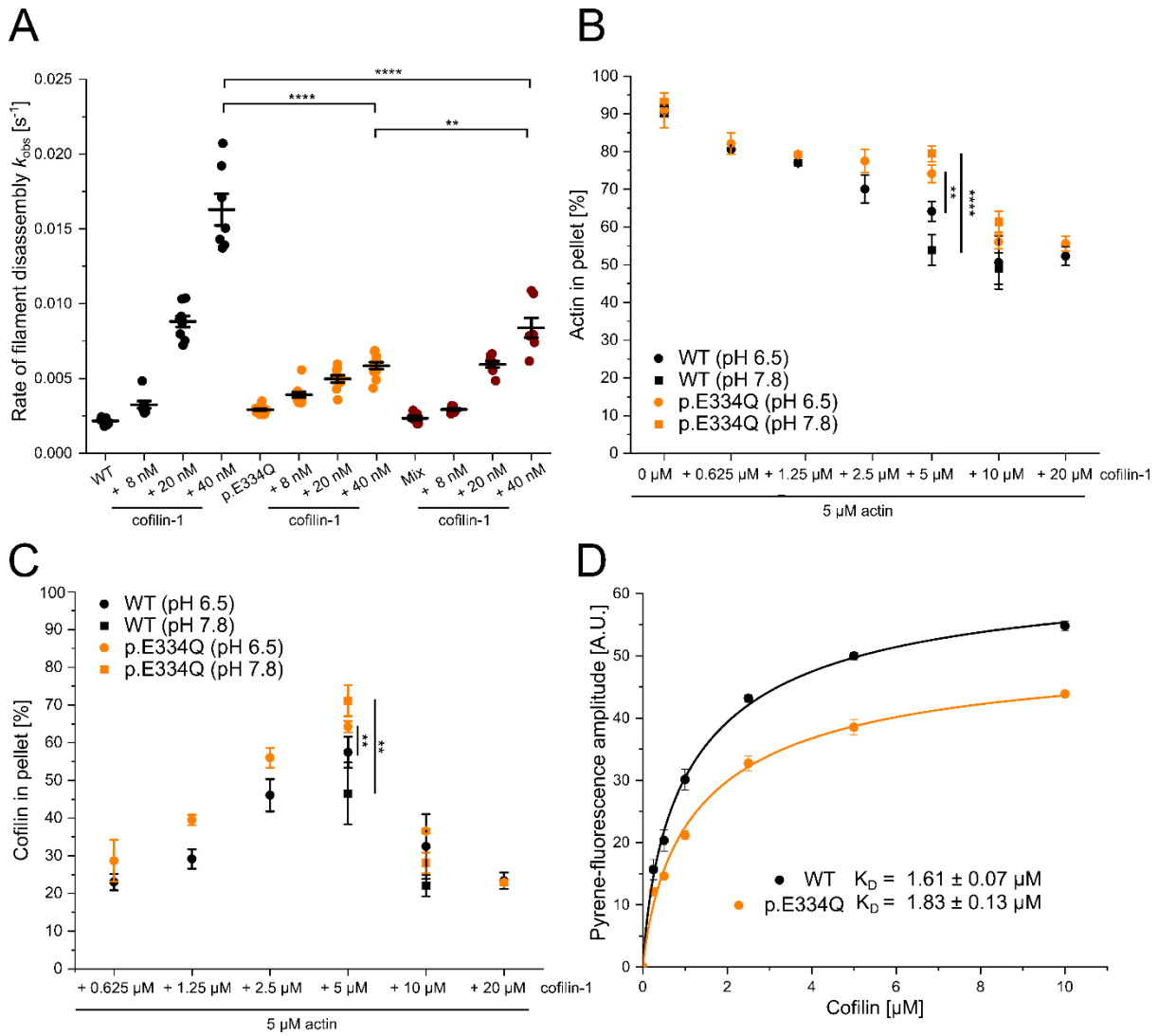

Figure 5 Analysis of the interaction of filamentous WT and p.E334Q γ–actin with cofilin–1. (A) Pyrene-based dilution–induced depolymerization experiments (5 % pyrene–labeled actin) were used to quantify the impact of cofilin–1 on the disassembly of filaments formed by p.E334Q, WT and a 1:1 mixture of p.E334Q and WT γ–actin. Depolymerization was induced by adding G–buffer (pH 7.8). Every data point represents an individual experiment. Data is shown as the mean ± SEM. **(B, C)** In addition, cofilin-1 mediated filament disassembly at different pH values (pH 6.5, pH 7.8) was investigated in co–sedimentation experiments. Shown are the means ± SEM of at least three individual experiments. **(D)** The dissociation equilibrium constant K_D for binding of cofilin-1 to pyrene-labeled WT or p.E334Q filaments was determined by monitoring the change in fluorescence amplitude upon cofilin-1 binding. Shown are the means ± SEM of at least three individual experiments.

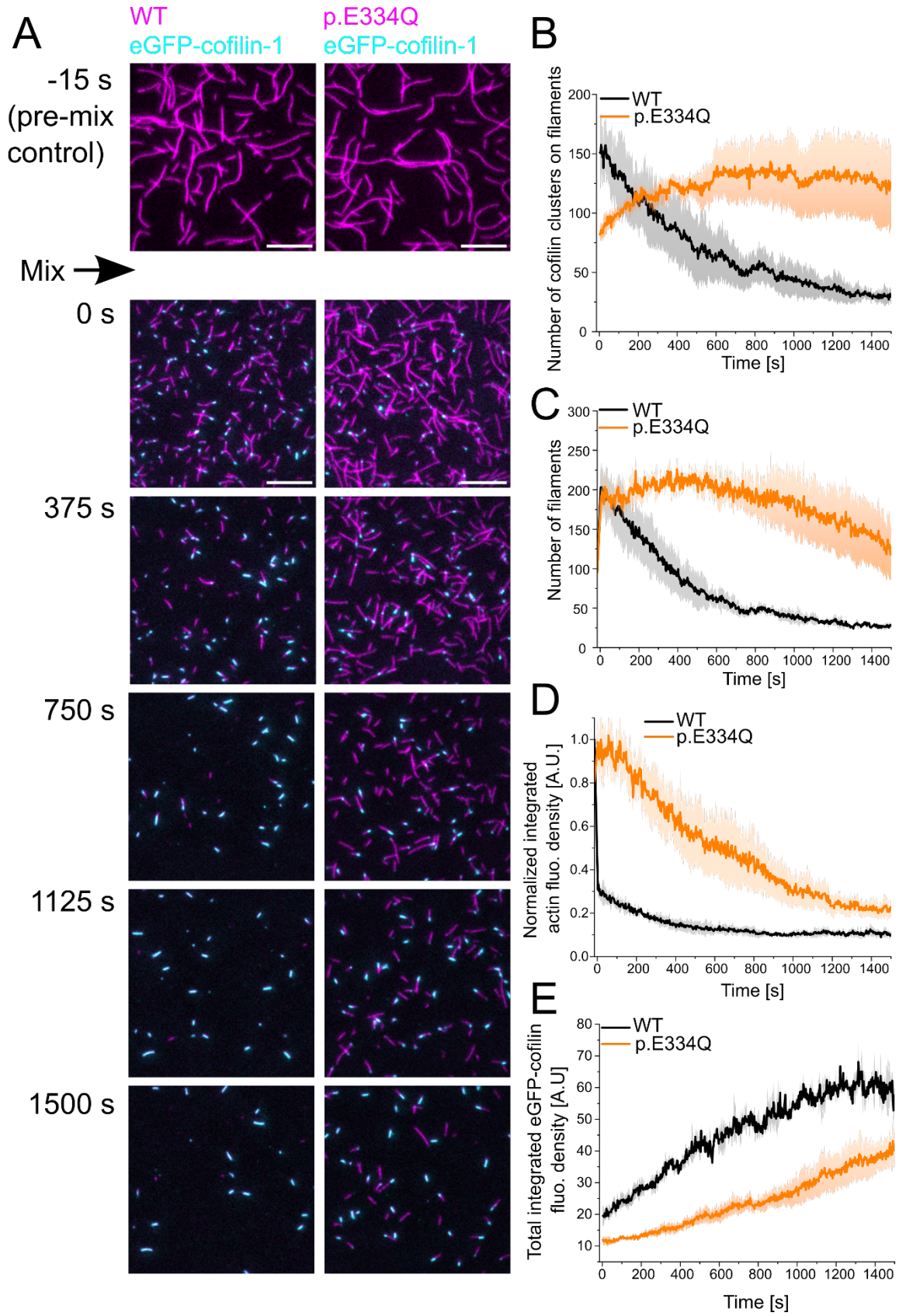

Figure 6 Analysis of the interaction of WT and p.E334Q γ–actin with eGFP–cofilin–1 (A) The disassembly of 300 nM "aged" WT and p.E334Q F–actin (10% Atto–655 labeled, capped by CP) in the presence of 100 nM eGFP–cofilin–1 was visualized using two–color TIRF microscopy. F–actin is shown in magenta, eGFP–cofilin in cyan. Shown are representative micrographs at the indicated time points.

1560 Scale bar corresponds to 10 µm. **(B)** Time dependence of the change in the number of eGFP–cofilin–1
1561 clusters on actin filaments. The solid lines and shades represent the mean ± SEM of three individual
1562 experiments. **(C)** Time dependence of the decrease in filament count. The solid lines and shades
1563 represent the mean ± SEM of three individual experiments. **(D)** Temporal tracking of actin filament
1564 disassembly by monitoring changes in total actin fluorescence per image frame. The solid lines and
1565 shades represent the mean ± SEM of three individual experiments. **(E)** Visualization of temporal
1566 changes in the abundance of eGFP–cofilin–1 clusters based on monitoring total eGFP–cofilin–1
1567 fluorescence per image frame. The solid lines and shades represent the mean ± SEM of three individual
1568 experiments.

1569

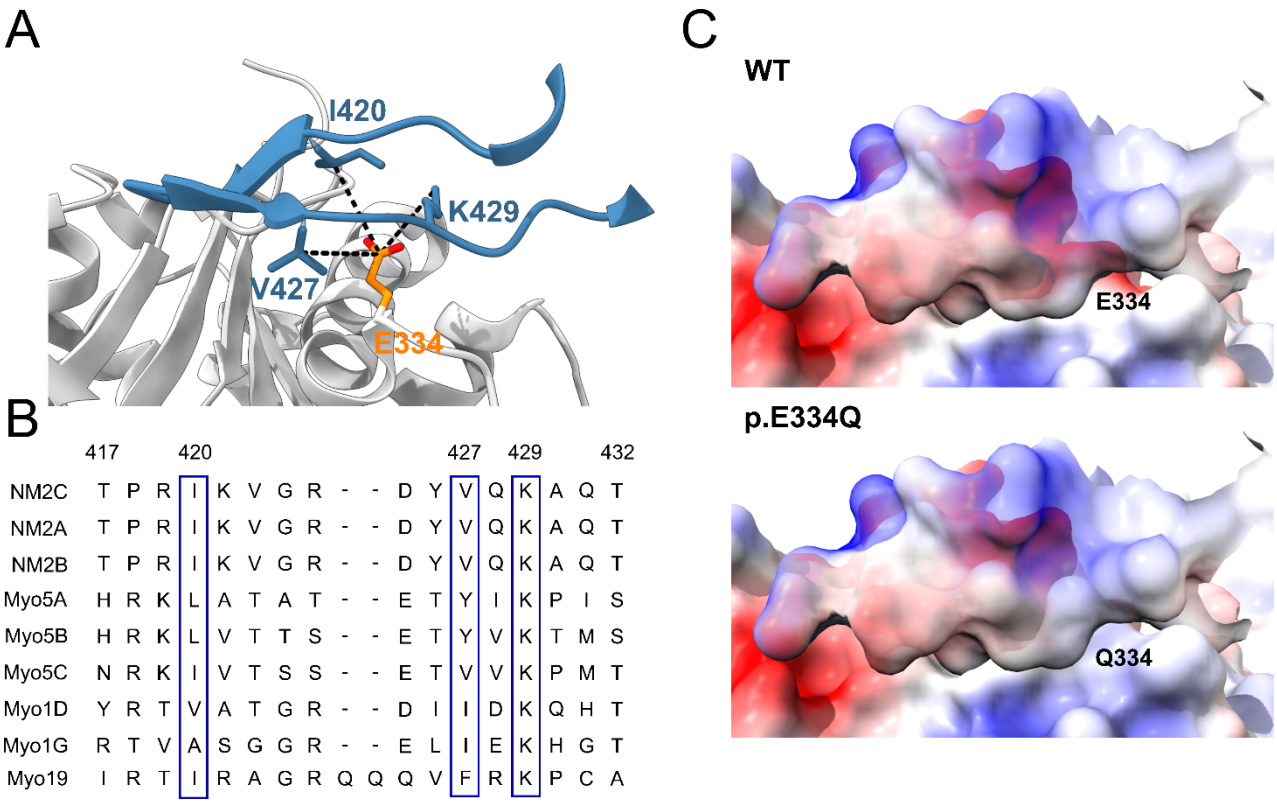

Figure 7 *In silico* analysis of the effects of the E334Q mutation on the actin–myosin interaction. (A) Contact region between the CM–loop of NM2C (blue) and residue E334 (orange) in cytoskeletal γ–actin (PDB–ID: 5JLH) (Von Der Ecken *et al*, 2016). Actin interacts with a core contact triad in the myosin CM-loop, which in the case of NM2C consists of lysine K429 and hydrophobic residues I420 and V427. **(B)** Multiple sequence alignment of the CM-loop of selected cytoskeletal myosin isoforms. The alignment shows complete sequence identity for NM2C, NM2A and conservation of residues contributing to the core contact triad in class 5, class 19 and selected members of class 1 myosins (blue boxes). Residue numbering refers to the NM2C primary structure. **(C)** Mutation E334Q leads to a weakening of complementary electrostatic interactions. The interaction interface involving the CM-loop of NM2C and the region affected by the mutation on cytoskeletal γ–actin is visualized by coulombic surface coloring. Positive potentials are shown in blue, and negative potentials in red.

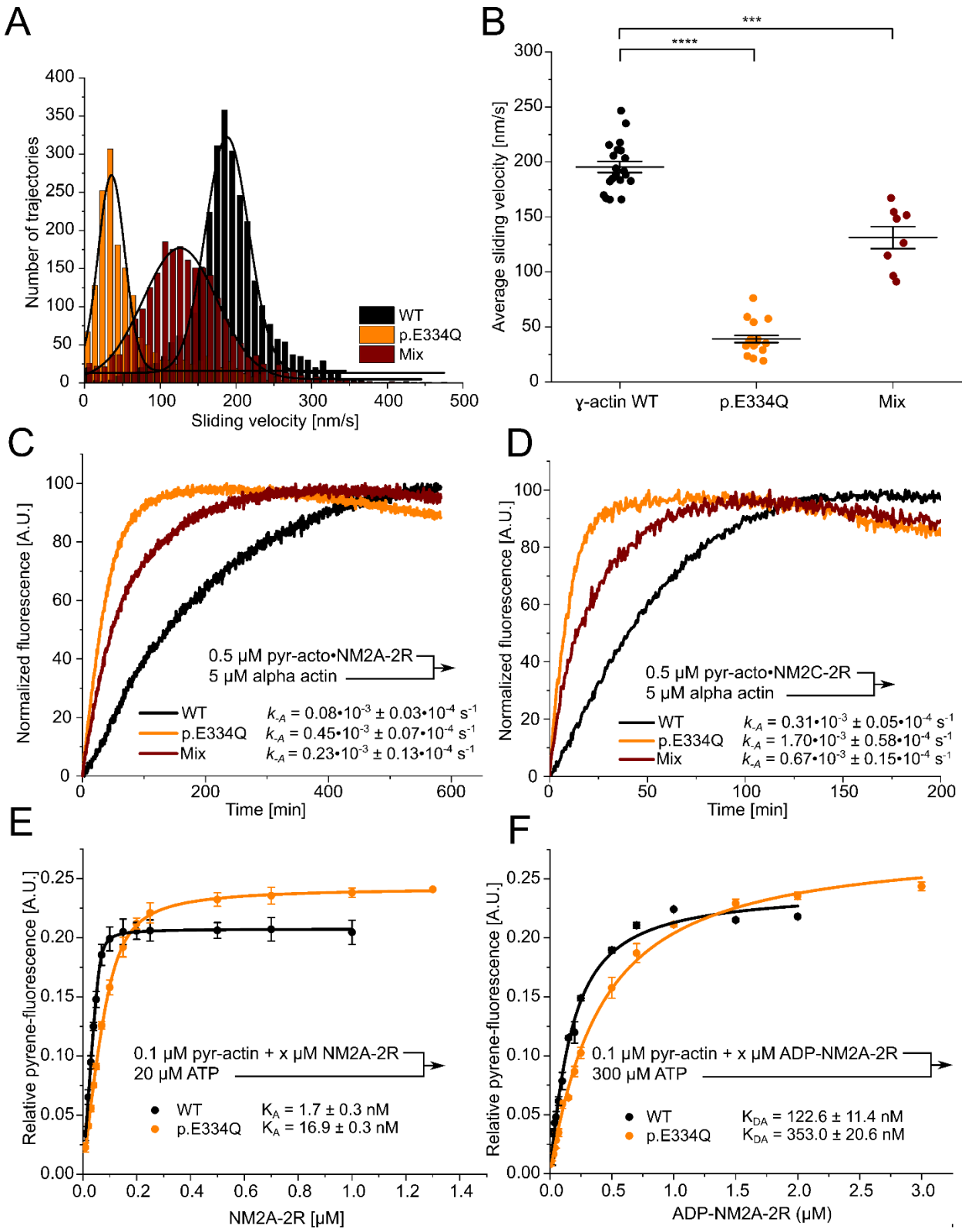

Figure 8 Analysis of the interaction of human NM2A with WT and p.E334Q γ–actin. (A) The interaction of surface–immobilized NM2A–HMM with WT γ–actin filaments, p.E334Q γ–actin filaments and heterofilaments (1:1 mixture) was analyzed using the unloaded *in vitro* motility assay. Representative velocity distributions are obtained from recorded trajectories of WT and mutant filaments in a single experiment. The average sliding velocity of the filaments in each experiment was determined by applying a Gaussian fit (black line) to the obtained velocity distributions. (**B**) Secondary plot of all measured sliding velocities. Each data point represents a single experiment (N=20 for WT filaments,

1591 N=18 for p.E334Q filaments, N=8 for heterofilaments) in which the sliding velocities of a minimum of
1592 600 filaments have been analyzed. The average sliding velocity in each experiment was determined as
1593 described in (A). **(C, D)** Determination of the dissociation rate constant (k_{-A}) for the interaction of
1594 NM2A–2R (C) or NM2C-2R (D) with p.E334Q or WT γ–actin in the absence of nucleotide. k_{-A} was
1595 determined in displacement experiments where unlabeled α–skeletal actin was added to pyrene–
1596 labeled acto•NM2A–2R/NM2C-2R. Shown are representative traces. The shown k_{-A} values are the
1597 results of 5–11 individual experiments using single–exponential fit functions. **(E, F)** The affinity of WT
1598 and p.E334Q γ–actin for NM2A–2R in the absence (K_A) and in the presence of saturating ADP
1599 concentrations (K_{DA}) was determined using the method developed by Kurzawa and Geeves (Kurzawa
1600 & Geeves, 1996). Increasing concentrations of myosin were dissociated from pyrene–labeled WT or
1601 p.E334Q F–actin by mixing the complex with excess ATP. The obtained fluorescence amplitudes of the
1602 individual transients were plotted against the corresponding myosin concentrations. A quadratic
1603 equation (see Material and Methods) was fitted to the data, which yields the respective affinity. Data
1604 is shown as the mean ± SD of three individual experiments.

1605

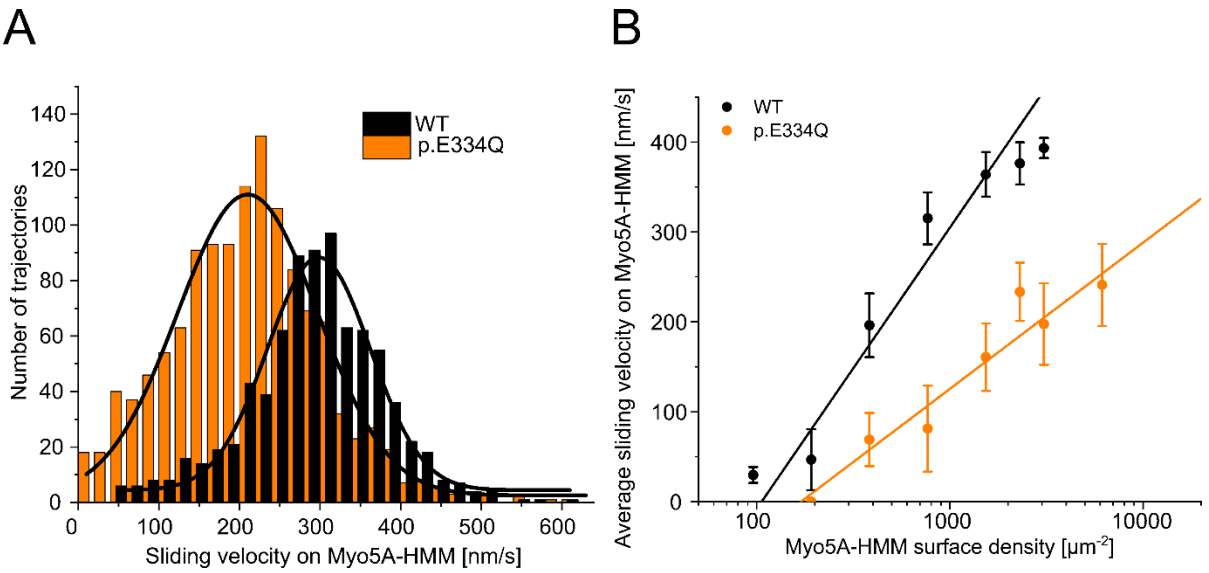

Figure 9 Analysis of the interaction of human Myo5A-HMM with WT and p.E334Q γ–actin in the unloaded *in vitro* motility assay at different Myo5A surface densities. (A) The interaction of surface–immobilized Myo5A–HMM with WT γ–actin and p.E334Q γ–actin filaments was analyzed using the unloaded *in vitro* motility assay. Representative velocity distributions were obtained from one individual experiment at the optimal Myo5A-HMM surface density for WT (770 μm^{-2}) and p.E334Q filaments (3100 μm^{-2}). The average sliding velocity of the filaments in each experiment was determined by applying a Gaussian fit (black line) to the obtained velocity distributions. **(B)** Semi–logarithmic plot summarizing all measured sliding velocities at different Myo5A–HMM surface densities. Each data point is the result of 3–10 individual experiments. The dependence of the average sliding velocity on surface motor density is best–described in the semi–logarithmic graph by lines up to approximately 1000 motors μm^{-2} for WT filaments and 7000 motors μm^{-2} for p.E334Q filaments.

1618 Supplementary Figures

1619

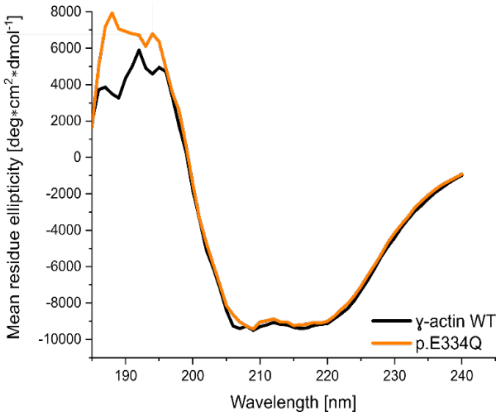

	α–helix	β–strand	Turns	Unordered	Total
γ–actin WT	22 %	24 %	22 %	31 %	99 %
p.E334Q	21 %	26 %	22 %	31 %	100 %

1620

1621 **Supplementary Figure 1** CD–Spectra of γ–actin WT and p.E334Q protein. Shown are the smoothed
1622 (Savitsky–Golay) and averaged spectra with the averaged buffer spectrum subtracted. The depicted
1623 secondary structure composition of γ–actin WT and p.E334Q protein was determined by using the
1624 DichroWeb online platform.

1625

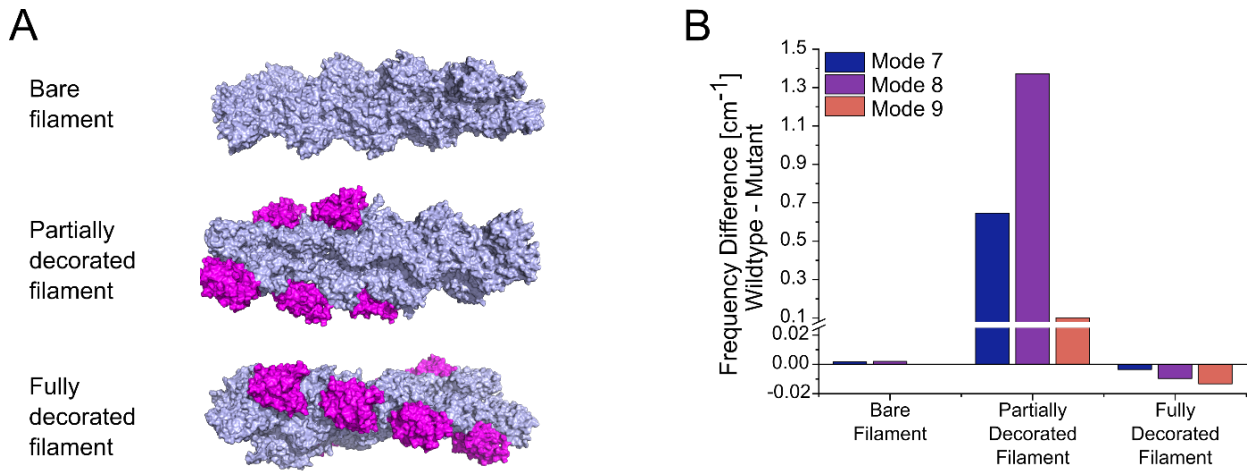

Supplementary Figure 2 Normal mode analysis of changes induced by mutation E334Q in the global mobility of bare, partially and a fully cofilin-1 decorated γ–actin mini-filaments (A) Models of a bare γ–actin mini-filament, a partially and a fully cofilin-1 decorated γ–actin mini-filament were generated for normal mode analysis. Each mini–filament consists of nine actin monomers. Actin is colored light blue and cofilin–1 magenta. **(B)** Significant differences in the global mobility of the different types of mini–filaments shown in panel (A), containing either WT or mutant cytoskeletal γ–actin, were only observed in the case of partial cofilin-1 decoration. Large differences are observed for partially decorated filaments in modes 7, 8 and 9, which are the global motions with the lowest frequencies.

1640

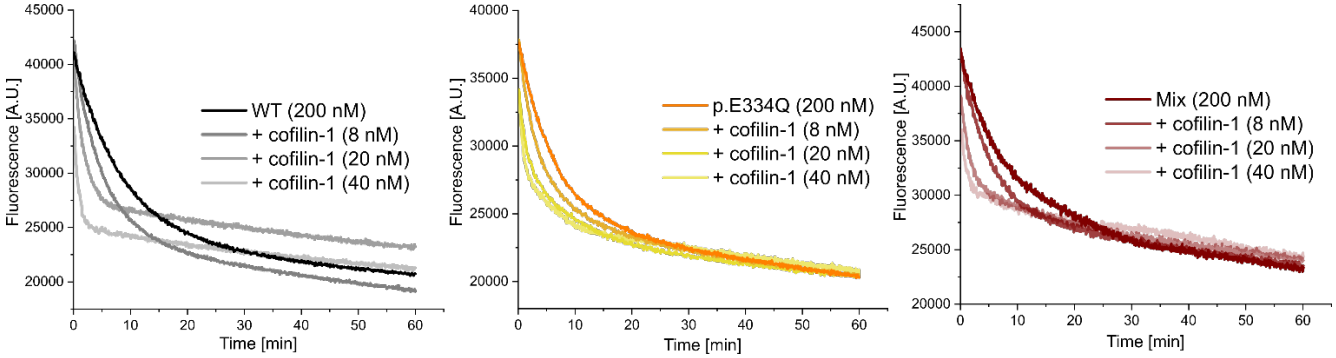

1641 **Supplementary Figure 3** Exemplary traces of dilution–induced depolymerization experiments in the
1642 absence and presence of increasing human cofilin–1 concentrations**.**

1643

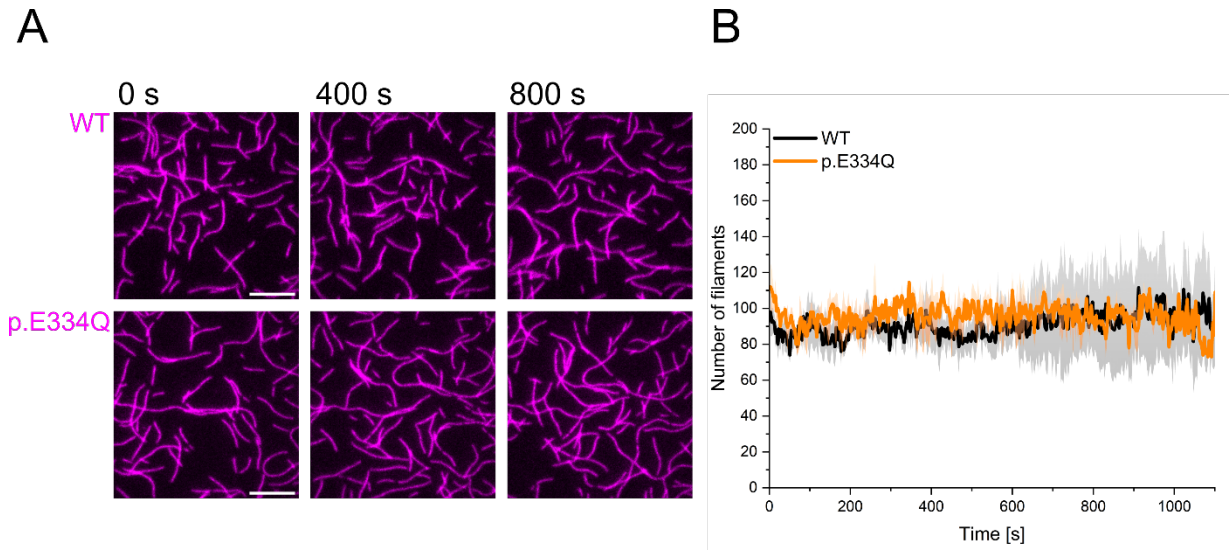

Supplementary Figure 4 (A) 300 nM "aged" WT and p.E334Q F–actin (10% Atto–655 labeled, capped by CP) was visualized using TIRF microscopy. Shown are representative micrographs at the indicated time points. Scale bar corresponds to 10 µm. **(B)** Quantification of the number of actin filaments over the time of the experiment. The solid lines and shades represent the mean ± SEM of 2–3 individual experiments.